UCLA
UCLA Electronic Theses and Dissertations

**Title**
Modulation Index Boosting -- Overcoming the Electrooptic Modulation Bottleneck

**Permalink**
https://escholarship.org/uc/item/7n26r5q6

**Author**
Borlaug, David

**Publication Date**
2016

Peer reviewed|Thesis/dissertation

eScholarship.org Powered by the California Digital Library
University of California

UNIVERSITY OF CALIFORNIA

Los Angeles

# Modulation Index Boosting

# Overcoming the Electrooptic Modulation Bottleneck

A dissertation submitted in partial satisfaction of the

requirements for the degree Doctor of Philosophy

in Electrical Engineering

by

David Borlaug

2016

© Copyright by

David Borlaug

2016

ABSTRACT OF THE DISSERTATION

Modulation Index Boosting

Overcoming the Electrooptic Modulation Bottleneck

by

David Borlaug

Doctor of Philosophy in Electrical Engineering

University of California, Los Angeles, 2016

Professor Bahram Jalali, Committee Chair

Electronic systems are dominant in information processing, display, and storage. However, optical systems are needed for broad-band long distance communication, antenna remoting, filtering, sensing, and imaging. Conventional high-performance electro-optic modulators, which place electronic information on optical waves, are the bottleneck of optical communication links and photonic time-stretch analog to digital converters, suffering a trade-off between low-voltage operation and large microwave bandwidths.

Unfortunately, the development of EO modulators has not kept up with the tremendous pace of electronics over the past decades. To be sure, access to broadband optical channels is curtailed by the limited bandwidth of EO modulators which are currently available in the 35 GHz range. Furthermore, the required drive voltage is currently in the 2-5 V range, a value that increases with speed. While EO modulators with 100Gbps capacity (~70GHz analog bandwidth)

are being developed, their bandwidth is approaching the fundamental limit imposed by velocity mismatch between electrical and optical waves in the traveling wave electrode. This is in direct conflict with the trend in electronics in which the voltage swing continues to decrease with increasing transistor speed. It is then clear that the current EO modulator technology is unable to meet the requirements of future systems.

This dissertation focuses on an exciting new concept that exploits modulation instability, a nonlinear optical process, to compensate for the intrinsically weak $\chi^{(2)}$ electro-optic effect. The technique, known as Modulation Index Boosting or MiBo, can be exploited to boost the weak electrooptic effect, one of the most fundamental and pressing predicaments in optical communication. In the approach, modulation sidebands stimulate MI in a third order $\chi^{(3)}$ nonlinear optical material placed after the electrooptic device. This effect enhances the $\chi^{(2)}$ of the electrooptic modulation material and also compensates for the device related high frequency roll-off. Boosting the $\chi^{(2)}$ of one material with the $\chi^{(3)}$ -induced MI of another material is an intriguing concept that enables low voltage electrooptic modulation at ultrahigh frequencies. Such a technology could provide a tremendous capability enhancement to high-speed digital, analog, SIGINT, and radar systems.

The dissertation of David Byron Borlaug is approved.

Eric Pei-Yu Chiou

Oscar Stafsudd

Bahram Jalali, Committee Chair

University of California, Los Angeles

2016

Table of Contents

1. Introduction.....1

2. Theory of Modulation Index Boosting.....6

3. Proof of Principle Simulations.....13

4. Experimental Demonstration of Vpi reduction.....16

5. Experimental Demonstration of Sub-Octave Linearity.....20

6. Advanced Simulations.....23

7. Phase Modulation.....37

8. MiBo prototype.....38

9. Time-Stretch MiBo.....44

10. Photon Doppler Velocimetry.....50

11. Conclusion.....64

12. References.....65

Acknowledgments

It is simply not possible to adequately acknowledge the tremendous support and encouragement I have received over the course of my doctoral work. However, the following few words serve as a small measure of my appreciation.

Prof. Bahram Jalali has been a tremendously insightful and motivational advisor, to which I am truly grateful. Prof. Jalali, thank you for your continued dedication and excellence in academic research, scientific market analysis, and pedagogical methods. It has been my honor to be your student.

I am fortunate to have the advice and counsel of a fantastic committee. My sincere thanks to Dr. Bill Seng, Prof. Eric Pei-Yu Chiou, Prof. Tatsuo Itoh, Prof. Oscar Stafsudd, and Prof. Bahram Jalali for agreeing to serve on my committee and for your guidance and helpful comments.

I must offer my sincere appreciation to Dr. Bill Seng and Dr. David Williams of Sandia National Laboratories, who generously funded my doctoral work through a graduate student fellowship. Additionally, I was honored to spend two summers on site at Sandia in Albuquerque, NM. During this time I had the outstanding opportunity to work alongside Sandia scientists under the pleasantly graceful and intensely stimulating advisement/management of Dr. Seng. Thank you Dr. Seng and Dr. Williams for your support.

I'd like to thank all members of the Jalali-lab, both past and present. I would like to especially thank Dr. Mohammad Asghari for insightful and inspiring technical discussions, Dr. Peter DeVore for early collaboration on the MiBo project, Dr. Varun Raghunathan with whom I

performed my first free-space optical experiments, and Cejo Konuparamban Lonappan who's patient (and insistent) encouragement and support in switching to linux-based computing has changed my life for the better.

The graduate student affairs manager, Deeona Columbia along with her support staff Mandy, Ryo, and others are a critical and central component of what makes the UCLA engineering department the great department it is. Thank you for your day in day out professionalism and support.

I would also like to thank the staff at UCLA's CNSI clean room. The CNSI facility is a first-rate academic clean room facility and I was fortunate to use the many fantastic tools there, as well as experience the broad support of Ghassan Malek and Tony Wright.

Finally, my greatest thanks must go to my wife and the love of my life, Amy Cordero, who is a daily source of joy and inspiration, without which I surely would not have completed this program. Thank you Amy for your support.

* * * * *

Large portions of this work are based on research authored by David Borlaug, performed under the advisement of Prof. Bahram Jalali see "Publications and Presentations". In particular:

- Chapter 1 borrows heavily from "Enhancing electrooptic-modulators using modulation instability," Phys. Status Solidi RRL 7, 566 (2013); "Enhancing Electrooptic-Modulators

Using Modulation Instability," a proprietary proposal submitted to DARPA in 2013; "THz Electrooptic Modulators" a proprietary proposal submitted to ONR in 2012.

- Chapter 2 borrows heavily from "Enhancing electrooptic-modulators using modulation instability," Phys. Status Solidi RRL 7, 566 (2013).
- Chapter 4 borrows heavily from "Demonstration of Vpi Reduction in Electrooptic Modulators using Modulation Instability," IEEE Photonics, Vol. 6 No. 5 (2014).
- Chapter 5 borrows heavily from "Vpi Reduction by Using Modulation Index Booster (MiBo) in RF Links," Optical Interconnect Conference, WD5, (2015).
- The Abstract and Conclusion borrow heavily from all of the above.

## Biographical Sketch

David Byron Borlaug earned a Bachelors of Science in Electrical Engineering at the University of California, Santa Barbara in 2006. In 2008, he earned a Masters of Science in Electrical Engineering at the University of California, Los Angeles. From 2008 to 2011 David served as a senior technical consultant at Booz Allen Hamilton where he supported various programs in the optical sciences at the Defense Advanced Research Projects Agency (DARPA). In 2011 David enrolled in a PhD program at the University of California, San Diego before transferring to the University of California, Los Angeles in 2012 to complete his PhD studies. In 2014 David was elected to serve as the general chair of the nonlinear optics technical group for the Optical Society of America (OSA). David is a member of the OSA and IEEE.

## Selected Publications

Selected Archival Journal Publications


[1] Huashun Wen, **David Borlaug**, Hongxiang Wang, Yuefeng Ji, Bahram Jalali, "Engineering Strain in Silicon Using SIMOX 3-D Sculpting," IEEE Photonics Journal, Volume 8, Number 2, (2016). doi:10.1109/JPHOT.2016.2535909.

[2] **David Borlaug**, Peter T. S. DeVore, Ali Rostami, Ozdal Boyraz, and Bahram Jalali, "Demonstration of Vpi Reduction in Electrooptic Modulators using Modulation Instability," IEEE Photonics, Vol. 6 No. 5 (2014). doi:10.1109/JPHOT.2014.2352626.

[3] Peter T. S. DeVore, **David Borlaug**, and Bahram Jalali, "Enhancing electrooptic-modulators using modulation instability," Phys. Status Solidi RRL 7, 566 (2013). doi:10.1002/pssr.201307174.

[4] **D. Borlaug**, R. R. Rice, and B. Jalali, "Raman Beam Cleanup in Silicon in the Mid-Infrared," Opt. Express 18(12), 12411-12414 (2010). doi:10.1364/OE.18.012411. arXiv:1002.4675.

[5] **D. Borlaug**, S. Fathpour, and B. Jalali, "Extreme Value Statistics in Silicon Photonics," IEEE Photonics Journal 1(1), 33-39 (2009). doi:10.1109/JPHOT.2009.2025517. arxiv:0809.2565.

[6] V. Raghunathan, **D. Borlaug**, R. R. Rice, and B. Jalali, "Demonstration of a Mid-infrared silicon Raman amplifier," Opt. Express 15(22), 14355-14362 (2007). doi:10.1364/OE.15.014355.

Selected Conference Proceedings

[7] **David Borlaug**, Rasul Torun, Ozdal Boyraz, and Bahram Jalali, "Vpi Reduction by Using Modulation Index Booster (MiBo) in RF Links," Optical Interconnect Conference, WD5, (2015). doi:10.1109/OIC.2015.7115729.

[8] **D. Borlaug**, P. DeVore, and B. Jalali, "Demonstration of Vpi Reduction in Electrooptic Modulators using Modulation Instability," IEEE Summer Topicals Meeting Series, WD2.3, Montreal, (2014). email:dborlaug@ucla.edu.

[9] **D. Borlaug**, P. DeVore, and B. Jalali, "Experimental Demonstration of Vpi Reduction in EO Modulators using Modulation Instability," in proceedings of Conference CLEO: 2014, OSA Technical Digest (online) (Optical Society of America, 2014), paper SM1G.4, (2014). doi:10.1364/CLEO_SI.2014.SM1G.4.

[10] V. Raghunathan, **D. Borlaug**, R. Rice, and B. Jalali, "Mid-Infrared Silicon Raman Amplifier," in proceedings of Advanced Solid-State Photonics (ASSP), Nara, Japan, TuB1, (2008). doi:10.1364/ASSP.2008.TuB1.

## 1. Introduction

Electrooptic (EO) modulation is the critical bridge that connects electronics to optics [1], [2]. While today's communication, sensing and computing systems are predominantly electronic, optics is indispensable by virtue of its unique functionalities including (1) wideband data capacity and interconnects, (2) wideband amplification, filtering, bandwidth elasticity (time stretch and time compression), (3) biochemical spectroscopy and sensing, and (4) imaging and display functions. The ability to seamlessly convert electronic to optical signals is therefore a critical function in future systems in which electronics and optics must coexist.

In the past, electrooptic devices were much faster than electronics so the EO conversion was not a bottleneck. However, electronics' extraordinary rate of progress, popularly known as Moore's Law, has now tipped the scale such that the EO converter is not only the speed bottleneck but also is incompatible with modern electronics from the voltage swing perspective as well as material compatibility. While transistor cutoff frequencies have approached 500 GHz and circuits with >100GHz bandwidth are now available, the fastest commercially available EO modulators are limited to approximately 40 Gbps, or roughly 30 GHz analog bandwidth [2]. These EO modulator speeds are achieved at the cost of increased modulation voltage brought about by the decline of electro-optic interaction due to the increased loss of metallic electrodes at high frequencies.

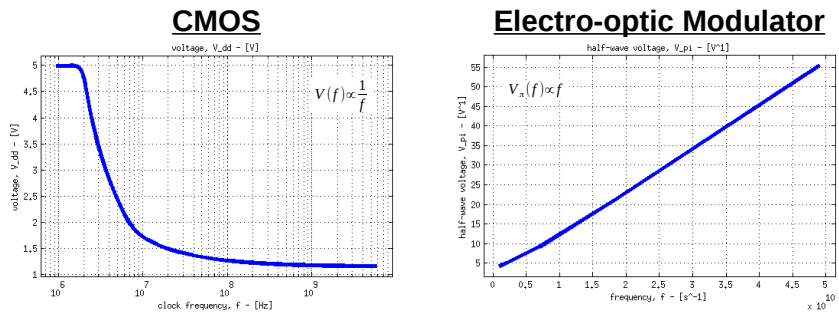


*Figure 1: Opposing voltage scaling trends create an information bottleneck. CMOS voltages reduce as frequency increases (left-side) [3]. EO-modulator voltages increase as frequency increases (right-side).*

As the electronic frontier continues to progress toward the terahertz regime, the modulator bottleneck will become more pronounced. Existing approaches for improving EO modulators are primarily focused on overcoming the RC time constant and increasing the interaction length between optical and electrical waves using traveling wave electrodes [1]. While these have achieved improved frequency responses, the progress has come at the cost of increased electrical drive voltage due to the shorter interaction length required for these bandwidths [4]. In addition, EO modulator bandwidth is approaching the fundamental limit imposed by velocity mismatch between electrical and optical waves in the traveling wave electrode. As a result, conventional devices can be designed for either low voltage or high frequency, but not both.

This is in direct conflict with the trend in electronics in which the voltage swing continues to decrease with increasing transistor speed. Unfortunately, the voltage reduction trend in electronics is brought about by a fundamental limitations due to dielectric breakdown and thermal density. In order to increase transistor frequency, a transit time limited gate length must be decreased. To keep the same electric field across the gate, necessary to avoid dielectric breakdown, the source-drain voltage must be reduced (c.f. Figure 1). However, transistor voltages are already near their lower limit as set by semiconductor physics, so channel electric

fields are increasing with increasing transistor frequencies. Therefore, dielectric material breakdown limits transistor voltage-frequency scaling.

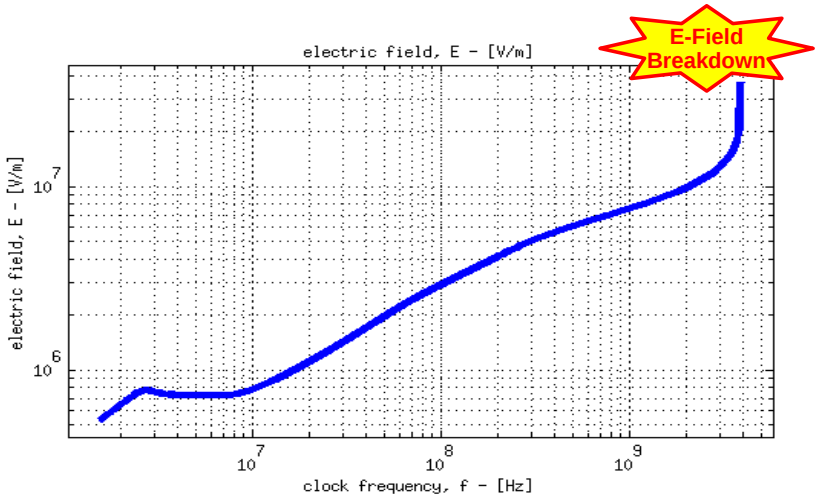


*Figure 2: As transistor frequencies increase, the electric field in the transistor gate is trending toward dielectric breakdown. Therefore, improvements in electronic operating frequencies will necessarily require further reduction in the transistor switching voltage to avoid breakdown.*

Additionally, as transistors continue to shrink and are packed more densely, the thermal load density also increases. The dominant approach to reducing this thermal load, proportional to $CV^2/2$, is to reduce the switching voltage.

In addition, both analog and digital optical communication systems must carefully consider the link's overall signal to noise ratio as governed by the link noise figure. Noise figure plays a limiting role in digital and analog error-free transmission over distance, as well as limiting the minimum detectable signal for short-run and instrumentation-focused analog systems. Careful link analysis shows the noise figure is a function of the modulator's half-wave voltage, $V_\pi$ [5].

$$NF = 10\log_{10}(F)$$

$$F = 1 + constant + \frac{4V_\pi^2}{\pi^2 r_d^2 T_{ff}^2 P_I^2 R_S^2} + \frac{V_\pi^2 RIN}{\pi^2 k T_0 R_S} + \frac{4qV_\pi^2}{\pi^2 k T_0 r_d T_{ff} P_I R_S} \tag{1}$$

$$F \propto V_\pi^2$$

Not only does a large $V_\pi$ deleteriously impact the noise figure, increasing the minimum detectable signal of analog optical links, but the unfortunate increase of $V_\pi$ as a function of frequency rapidly erodes the SNR for broadband systems.

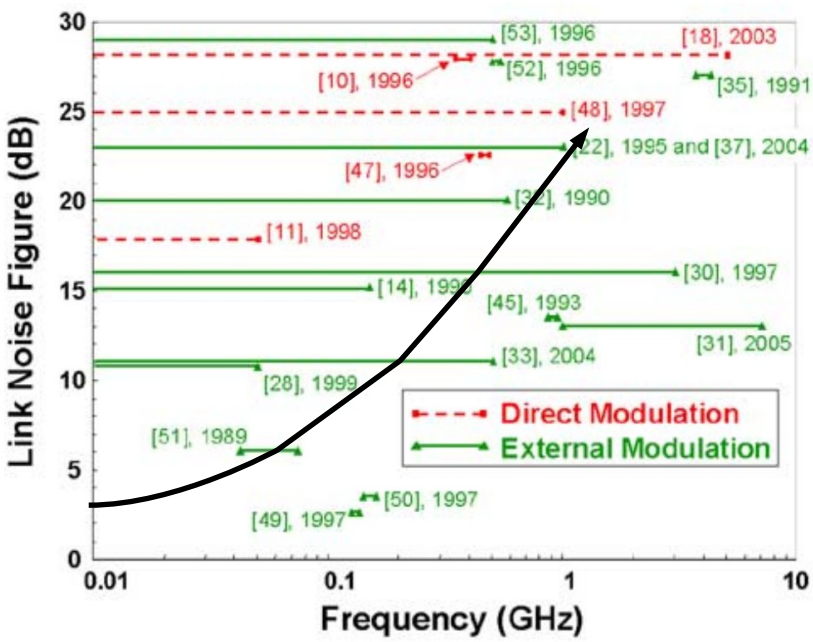


*Figure 3: Link Noise Figure is increasing as a function of frequency due to the modulator's large half-wave voltage. Reproduced from [5], with added trend-line.*

Therefore, if electronic drivers such as CMOS and other technologies were somehow able to produce the large voltages necessary to drive conventional modulators, the resulting link noise figure would be prohibitively large at higher frequencies.

It is then clear that the current EO modulator technology is unable to meet the requirements of future systems. This dissertation focuses on an exciting new concept that exploits modulation instability, a nonlinear optical process, to compensate for the intrinsically

weak $\chi^{(2)}$ electro-optic effect. The technique, known as Modulation Index Boosting or MiBo, can be exploited to boost the weak electrooptic effect, one of the most fundamental and pressing predicaments in optical communication. In the approach, modulation sidebands stimulate MI in a third order $\chi^{(3)}$ nonlinear optical material placed after the electrooptic device. This effect enhances the $\chi^{(2)}$ of the electrooptic modulation material and also compensates for the device related high frequency roll-off. Boosting the $\chi^{(2)}$ of one material with the $\chi^{(3)}$ -induced MI of another material is an intriguing concept that enables low voltage electrooptic modulation at ultrahigh frequencies. The technology is compatible with chip-integrated platforms, and can be utilized to enable advanced functionality in addition to boosting, including waveform manipulation and control. Such a technology could provide a tremendous capability enhancement to high-speed digital, analog, SIGINT, and radar systems.

The dissertation is organized as follows. Chapter 2 introduces the concept and theory of modulation index boosting. Chapter 3 includes preliminary simulations which demonstrate the concept numerically. Chapter 4 details the first experimental demonstrations. Chapter 5 presents experimental investigations into the linearity and minimum detectable signal of MiBo. Chapter 6 numerically investigates the MiBo approach using detailed component routines modeled after state-of-the-art commercial offerings. Chapter 7 contains information on a second-generation field-ready prototype, including the physical design and measured performance. Chapter 9 describes a new concept of incorporating MiBo with Time-Stretch technology, known as Time-Stretch MiBo. Chapter 10 investigates the benefits of incorporating MiBo into Pulsed Doppler Velocimetry systems. In chapter 11 the dissertation concludes with some final comments.

## 2. Theory of Modulation Index Boosting

Modulation instability (MI) is a nonlinear physical process whereby tiny disturbances spontaneously grow on an otherwise quiet background [6]. First discovered in hydrodynamics where it is known as the Benjamin-Feir effect [7], MI arises in diverse contexts such as sand-dune formation [8], free electron lasers [9], optics [10], and matter-waves [11], and has been described as “one of the most ubiquitous types of instabilities in nature” [12]. This process has been proposed as the mechanism that gives rise to oceanic rogue or freak waves [13], giant “walls of water” [14] that appear suddenly even out of calm seas [15]. Discovery of their optical counterpart, optical rogue waves [16], confirmed that specific noise stimulates their generation via MI. Purposefully stimulating the creation of optical rogue waves has led to enhanced bandwidth, stability and brightness [17][18][19][20] of the nonlinearly broadened light known as supercontinuum [21].

In this dissertation, a new concept known as Modulation Index Boosting (MiBo) is proposed as a path to broadband low-voltage electro-optic modulation. The method enhances any intensity modulator including those based on electro-refraction as well as electro-absorption effects. The booster is capable of reducing a Mach-Zehnder modulator's half-wave voltage, known as $V_\pi$, as well as extending its bandwidth by exploiting the intrinsic frequency dependence of the MI gain spectrum.

Modulation instability in optics results from the interplay between Kerr nonlinearity and anomalous group velocity dispersion. The effect can be obtained using linear stability analysis performed on analytical solutions to the nonlinear Schrödinger equation:

$$\frac{\partial A(z,t)}{\partial z}=\frac{-\alpha}{2}A(z,t)+\sum_{k\geq 2}\frac{i^{k+1}}{k!}\beta_k\frac{\partial^k A(z,t)}{\partial t}$$
$$+i\gamma(1-f_R)A(z,t)|A(z,t)|^2 \tag{2}$$
$$+i\gamma f_R A(z,t)\int_{-\infty}^{t}h_R(t-t')|A(z,t')|^2 dt'$$

where $A(z,t)$ is the field amplitude, $\beta_k=\partial^k\beta/\partial\omega_0^k$ are the dispersion coefficients, $\gamma=3\pi\chi^{(3)}/(4\lambda_0 A_{eff})$ is the Kerr nonlinear coefficient, $A_{eff}$ is the effective modal area, $n$ is the refractive index, $\lambda_0$ is the pump wavelength, $\alpha$ is the loss per unit length, and $f_R$ and $h_R$ are the Raman fractional contribution and response function respectively [6]. Over the electrically relevant pump-sideband frequency difference (< 1 THz), the Raman effect and dispersion terms $\beta_k$ with $k>2$ can be ignored. In general MI must be described using the rather complex dynamics of equation (2). For example, the full description provided by equation (2) is required to capture cases of temporally-confined MI [22], cases of MI with near-zero $\beta_2$ [23], or cases where the sidebands grow too large and deplete the carrier [24][25][26]. However, the initial evolution of MI from continuous-wave radiation with sizable anomalous group velocity dispersion $\beta_2$ can be described analytically using considerably simpler relationships. The sideband gain per unit length under this condition without loss or pump depletion is [6]:

$$g(\omega)=|\beta_2\omega|\left[\frac{4\gamma P}{\beta_2}-\omega^2\right]^{1/2} \tag{3}$$

where $\omega$ is the pump-sideband frequency separation and $P$ is the pump optical power. Here, sidebands modulated on a strong optical carrier utilize the carrier as the pump and are thus amplified to increase their modulation depth. The response of typical EO modulators is characterized by a high frequency roll-off resulting from electrode microwave losses and from

velocity mismatch between the microwave and the optical waves in the traveling-wave electrodes. The losses are primarily due to the skin effect, and radiative and dielectric loss (from waveguide scattering imperfections and molecular resonances, respectively) [27]. **Fortuitously, the increase of MI gain with pump-sideband frequency separation compensates the modulator's high frequency roll-off, enhancing both the bandwidth and the EO sensitivity (c.f. Figure 4b)**. Figure 4c clearly shows the growth of a 100 GHz sideband as a function of booster length. The gain spectral width depends on fiber dispersion, fiber nonlinearity, and optical power, and span tens of GHz to >10 THz [6]. Therefore this technique is applicable to both narrowband (sub-octave) as well as broadband (multi-octave) intensity-modulated waveforms.

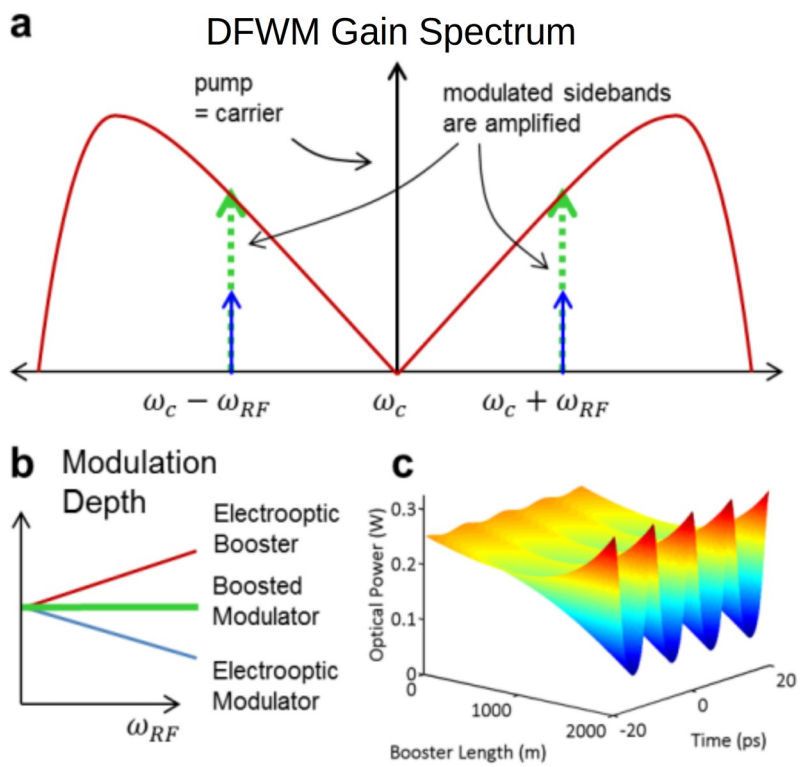


*Figure 4: (a) Modulation instability (MI) gain spectrum vs. optical frequency. Sidebands modulated on a strong optical carrier grow as a result of MI. The gain increases with modulation frequency. The broadband gain spectrum spans 10's of GHz. (b) Modulation depth vs. RF frequency. Increase in electro-optic booster MI gain with modulation frequency compensates electro-optic modulator roll-off, resulting in a low drive-voltage, wideband modulator. (c) Simulation of MI of a 100 GHz sideband demonstrates the strength of this concept.*

A general approach to characterize EO modulation can be derived from the transfer function for a Mach-Zehnder interferometer with an electro-optic element placed in one arm: $P_{out} = (P_{\text{in}}/2)\{1+\cos[\phi_0 + \pi(V/V_\pi)]\}$ where $P$ and $P_{out}$ are the optical powers before and after the modulator, respectively [1]. $V_\pi = s n \lambda_0 / (4\chi^{(2)}\Gamma \cdot l_{EO})$ is the half-wave voltage (with electrode separation $s$, EO overlap $\Gamma$, and EO interaction length $l_{EO}$), which is the characteristic voltage change required to induce a $\pi$ phase shift between the modulator arms [28]. $\phi_0$ is the static phase offset typically set to quadrature value ($\pi/2$). We consider

this modulator fed by a single frequency laser, and driven with a single-tone RF source, $\omega_{RF}$. Finally, the output of the modulator is detected by a square-law photodetector. The sidebands stimulate MI causing their growth at the expense of the carrier.

If $G$ is the sideband power gain, then sideband fields increase by $G^{1/2}$. As the detected RF current is a result of the carrier-sideband beating, the RF output power is proportional to the square of $G^{1/2}$, yielding:

$$P_{RF,out} \propto \frac{1}{V_\pi^2} P_{RF,\text{in}} G \tag{4}$$

where $V_\pi$ is the intrinsic Mach-Zehnder characteristic voltage, and $P_{RF,\text{in}}$ and $P_{RF,out}$ are the input and output RF powers. ***Here, by exploiting MI in a fiber that follows the Mach-Zehnder, the voltage required to achieve a given modulation depth is reduced***. From Eq. (4), the MI-induced growth of $P_{RF,out}$ by $G$ is equivalent to a $V_\pi$ reduction by $G^{1/2}$, yielding the boosted modulator half-wave voltage:

$$V_{\pi,eff}(\omega) = V_\pi(\omega) \frac{L_{dep}^{1/2}}{G^{1/2}(\omega)} \tag{5}$$

where $L_{dep} \leq 1$ is the pump (carrier) power depletion factor. **Equation (5) demonstrates both key abilities of the EO booster: (1) augmenting the modulator with modulation instability in a nonlinear fiber results in a lower "effective $V_\pi$", and (2) the EO booster effectively flattens the high-frequency roll-off of the modulator**. This can be interpreted as increasing the second order nonlinear susceptibility $\chi_{eff}^{(2)} = \chi^{(2)}(G^{1/2}/L_{dep}^{1/2})$. The desirable reduction of effective $V_\pi$ due to pump (carrier) depletion can be understood by recognizing that the transfer of power from the carrier to the sideband increases the ratio of AC to DC signal. Fortuitously, MI uses the carrier as the pump and so **requires no external power, providing an**

**energy efficient passive technique to increase modulation depth**. For communication applications, Eq. (5) enhances system performance, as calculated in the boosted shot-noise limited RF signal-to-noise ratio (SNR) [29]:

$$SNR = \frac{R_d Z_m P P_{RF,\mathrm{in}}}{4 q \Delta f} \frac{\pi^2}{V_{\pi,eff}^2} = [\frac{R_d Z_m P P_{RF,\mathrm{in}}}{4 q \Delta f} \frac{\pi^2}{V_\pi^2 L_{dep}}] G(\omega) \tag{6}$$

where $R_d$ is the detector photodetector responsivity expressed as the ratio of the photogenerated electrical current divided by the incident optical power, $Z_m$ is the electrical impedance of the modulator, $q$ is the elementary charge, and $\Delta f$ is the RF bandwidth.

The MI effect can be tuned to optimize the Shannon-Hartley channel capacity $C_B = \Delta f \log_2(1 + SNR)$ [30], the absolute upper bound on information transmission bit-rate, with RF bandwidth $\Delta f$. An analytical solution can be found if it is assumed that the noise is independent of MI gain (valid if pump-fluctuation transfer to the sidebands and MI-amplified quantum fluctuations can be neglected [31]), and that $SNR \gg 1$ (satisfied for any useful frequency band), as well as neglecting loss and pump depletion. The channel capacity can then be split into two terms, $C_B = C + \int \log_2[G(f)] df$, where $C_b$ and $C$ are the boosted and intrinsic channel capacities, respectively. To optimize the performance, one can tune the dispersion yielding the relation for the optimal MI cutoff frequency:

$$\Omega_C = \sqrt{\frac{4 \gamma P}{|\beta_2|}} = \omega_{high} \left\{ \frac{4[1 - (\omega_{low}/\omega_{high})^6]}{3[1 - (\omega_{low}/\omega_{high})^2]} \right\}^{1/4} \tag{7}$$

where $\omega_{low}$ to $\omega_{high}$ is the electrical RF signal bandwidth. Physically, this choice maximizes the logarithmic power over this band, the quantity of importance for information capacity. It is interesting to note that the form of the pre-boosted $SNR$ has no effect on how

the MI gain should be distributed. In the limit $\omega_{low} \rightarrow \omega_{high}$ (single frequency), $\Omega_c/\sqrt{2} \rightarrow \omega_{high}$ , as expected since this places the MI gain peak at the RF frequency of interest [6]. Substituting the optimal MI dispersion in the channel capacity relation yields:

$$C_B = C + \left[ \left( 1 - \frac{\omega_{low}^2}{\Omega_c^2} \right)^{3/2} - \left( 1 - \frac{\omega_{high}^2}{\Omega_c^2} \right)^{3/2} \right] \frac{2\gamma P l \Omega_c}{3\pi \ln(2)} \tag{8}$$

where is the EO booster length. If we consider the MI values below (which optimizes a frequency band from $f_{low} \approx 0$ to $f_{high} = 191[GHz]$ ), Eq. (8) predicts a stunning 4.7 bits/s/Hz added capacity in the ideal case. Although optical losses and added noise will reduce this in practice, the analysis does reveal the potential to strongly augment the information capacity of a communication link.

## 3. Proof of Principle Simulations

MI is simulated using the setup shown in Figure 5. A single-frequency $500[mW]$ laser and an ideal RF signal generator with impedance $Z_s = 50[\Omega]$ feeds a high-speed Mach-Zehnder modulator. The modulator is modeled [1][27] after Ref. [4] with active length $l_{EO} = 2[cm]$, $V_\pi = 5.1[V] for (\omega = 0)$, modulator impedance $Z_m = 47\Omega$, skin effect loss $\alpha_0 = 1.02 \times 10^{-4}[m^{-1} Hz^{-1/2}]$, and microwave and optical refractive indices $n_{RF} = 2.15$ and $n_{opt} = 2.14$ with optical loss ignored. The output of the modulator feeds an EO booster with $\alpha = 1[dB/km]$, $\beta_2 = -14[ps^2/km]$, $\gamma = 11.7[W^{-1} km^{-1}]$, attainable in commercial highly nonlinear fibers.

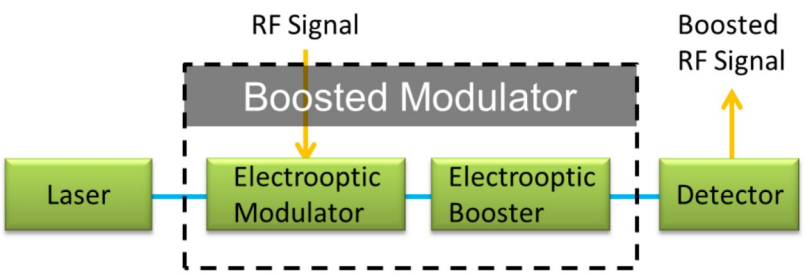


*Figure 5: Electro-optic booster in a communication link. The conventional link employs only the electro-optic modulator, while the boosted case shown here employs the added electro-optic booster, which uses MI gain to compensate modulation roll-off.*

The radiation is detected by an ideal photodetector with impedance $Z_d = 47[\Omega]$ and responsivity $R_d = 1[A/W]$. The nonlinear Schrödinger equation is solved by the split-step Fourier method [6], demonstrated to accurately capture nonlinear optical phenomena [19].

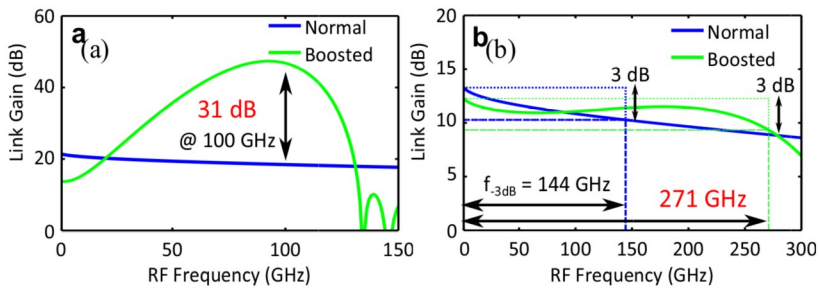


*Figure 6: Gain of normal and boosted communication links vs. RF frequency. (a) MI tailored for high gain at 100 GHz. Here the gain is improved 1000 times over the normal link. (b) MI tuned for bandwidth extension. MI's compensation of the roll-off nearly doubles link bandwidth from 144 GHz to 271 GHz.*

In Figure 6 we examine the normal and boosted link transfer function, $P_{\mathrm{RF,out}}(\omega)/P_{\mathrm{RF,in}}(\omega)$ , as an RF tone's frequency is varied. The MI gain response can be tailored via the EO booster parameters and laser power, here selected for large reduction (c.f. Figure 6a) and bandwidth extension (c.f. Figure 6b). In Figure 6a, a large negative group velocity dispersion is chosen for high-gain at 100 GHz, resulting in over 1000 times larger RF power than the normal link, vastly increasing sensitivity. Choice of smaller dispersion parameter (c.f. Figure 6b) increases the MI bandwidth, enabling near doubling of bandwidth from 144 GHz to 271 GHz.

The introduction of MI into a communication link raises concerns about noise. To be sure, MI has been identified as the source of noise in generation of supercontinuum (white light) radiation [21]. However, such fluctuations arise because in conventional supercontinuum generation, MI is spontaneously triggered by pre-existing noise. Indeed, it has been shown that when MI is stimulated by a deterministic yet minute seed, the output fluctuations are dramatically reduced by as much as 30 dB [19], effectively mitigating nondeterministic phenomena. In the proposed technique, the modulation sidebands that stimulate MI are phase-locked to the carrier; hence, the process will be inherently stable.

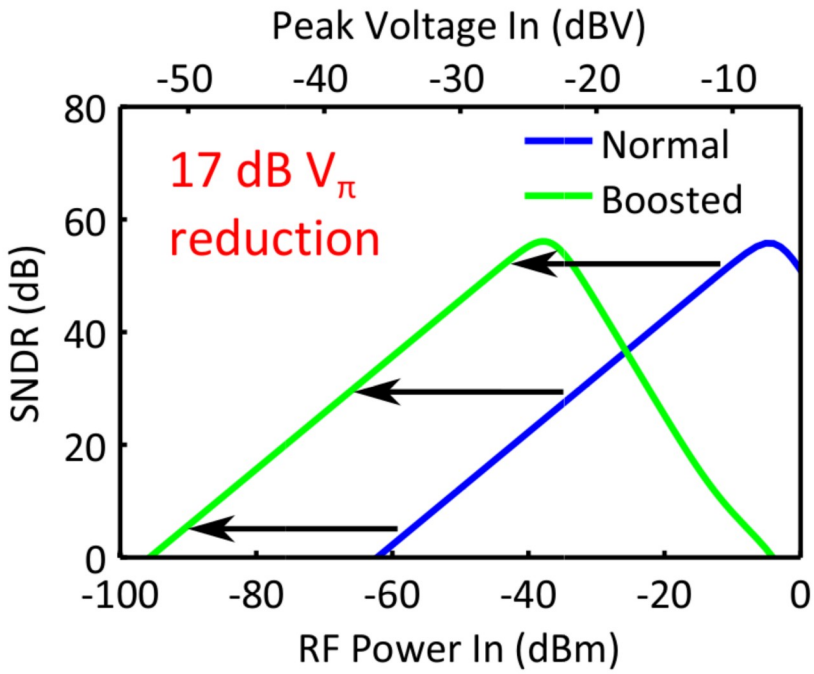


*Figure 7: Comparison between normal and boosted optical links. Signal to noise and distortion ratio (SNDR) [dB] is plotted vs. RF Power Input [dBm] and Peak Input RF Voltage [dBv] for the normal (blue) and boosted (green) case. Note the near identicality of the two traces showing distortion free operation. Also note that the input voltage requirement is reduced by 17 dB (or 50-fold) in the boosted case.*

The fidelity of the output RF signal is investigated using the signal to noise and distortion ratio (SNDR). Two RF tones, 100 and 101 GHz, are excited in the modulator and the detected photocurrent is bandpass filtered to 95 to 105 GHz with thermal and shot-noise included (c.f. Figure 7). The stability of the MI process stimulated by the deterministic sidebands is reflected in the lack of SNDR degradation for the boosted modulator in Fig. 5. The observed 17 dB shift in the SNDR thus implies over 50 times reduction of effective, from 6.7 V to 114 mV.

4. Experimental Demonstration of Vpi reduction

The experimental setup is shown in Figure 8. A tunable laser diode at 1550 nm feeds an isolator protected EDFA, the output of which is polarization aligned with a phase modulator that is driven by an amplified 500 MHz band-limited white noise source for stimulated Brillouin scattering (SBS) suppression.

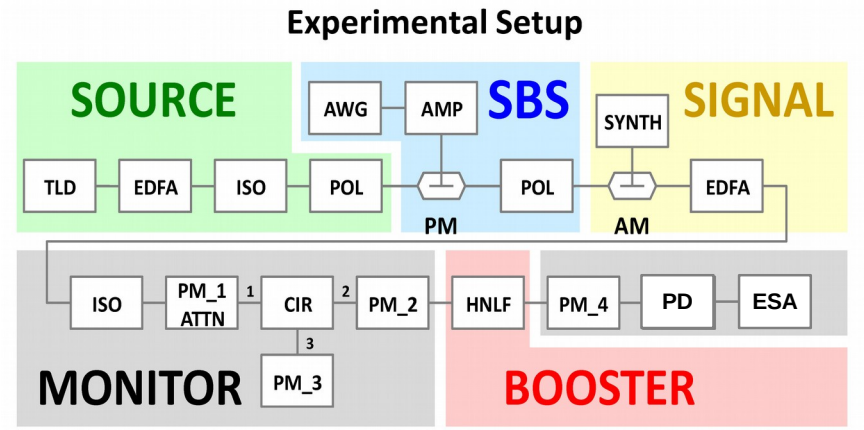


*Figure 8: Experimental setup. A continuous-wave laser source (SOURCE), acting as the carrier and pump, is phase modulated to prevent stimulated Brillouin scattering (SBS) in the BOOSTER. The RF signal is modulated onto the carrier (SIGNAL) and is boosted in the BOOSTER. The MONITOR measures the booster input power, output power, back-reflected power, and optical spectra. The MONITOR is therefore able to verify the limited impact of stimulated Brillouin scattering on the boosting process. TLD: tunable laser diode; EDFA: erbium doped fiber amplifier; ISO: isolator; POL: polarization controller; PM: phase modulator; AWG: arbitrary waveform generator; AMP: amplifier; AM: amplitude modulator; SYNTH: synthesizer; PM_[#]: power meter, numeric designator; CIR: circulator; HNLF: highly nonlinear fiber of 2 km length; PD: photodiode; ESA: electrical spectrum analyzer.*

The amplified noise source has a peak-to-peak voltage of 6.32 V and drives an EOSpace 10 GHz phase modulator, model number PM-0K1-10-PFU-PFU, having a half-wave voltage of 4.0 V at 1 GHz. The SBS suppressed carrier is polarization aligned with an EOSpace 20 GHz Mach-Zehnder modulator, model number AZ-1x2-0K1-20-PFU-SFU, having a half-wave voltage of 4.5 volts at 1 GHz. The amplitude modulator is driven by an HP 83650B synthesizer at RF frequencies from 1 to 49 GHz with 1 GHz granularity. The RF power input to the AM modulator

is kept constant at 1 mW. The modulated waveform is amplified by an isolator protected EDFA, variably attenuated, boosted by the highly-nonlinear fiber, and detected by an optical spectrum analyzer. At 1550 nm the HNLF is described by the following coefficients: $\alpha = 1[dB/km]$, $\beta_2 = -10.9[ps^2/km]$, $\beta_3 = 0.062[ps^3/km]$, and $\gamma = 11.6[W^{-1}km^{-1}]$. A circulator and various power monitors are used to precisely control the power before entering the HNLF and to monitor SBS suppression.

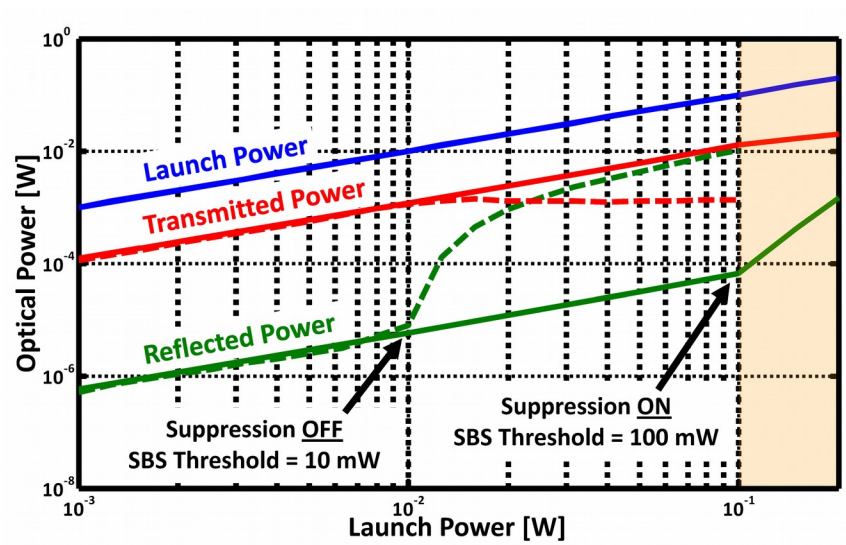


*Figure 9: Monitoring of SBS with suppression on (solid lines) and off (dashed lines). Note that the deviation from linear reflected power as a function of launch power occurs at 10 mW for the unsuppressed case and 100 mW for the suppressed case. With SBS suppression on, SBS is completely suppressed up to and including 100 mW launch powers. At 200 mW launch power 3.4 mW is reflected by SBS.*

Figure 9 shows the transmitted and reflected power as a function of the launch power with respect to the HNLF. These power levels correspond to PM_4, PM_3, and PM_2 of Figure 8, respectively. The launch power is set manually by adjusting the variable attenuator in PM_1/ATTN. Two cases are shown: (1) the case where SBS suppression is turned off as shown using the dashed line, and (2) the case where SBS suppression is turned on as shown using a solid line. As seen in the figure, SBS suppression is successful in regions that observe a linear

dependence between the reflected power and the launch power [32]. In the case of SBS suppression turned off, SBS onset begins beyond 10 mW launch power. In the case of SBS suppression turned on, SBS begins beyond 100 mW launch power. The approach achieves 10 dB of SBS suppression. Note that SBS will play no role in experiments utilizing launch powers up to and including 100 mW with SBS suppression turned on. At 200 mW launch power with SBS suppression turned on SBS causes a 3.4 mW back reflection and a 7 mW drop in transmitted power. Suppression of SBS is critical to ensuring observed modulation enhancement is due to MI, as desired. Past works have shown as high as 17 dB SBS suppression using similar approaches [32] with higher drive voltages.

Now that the SBS suppression capabilities are understood boosting measurements can proceed. A single RF tone is input in to the MiBo setup, and the received RF tone power is measured using the ESA. By sweeping the tone frequency, the MiBo RF Power gain and RF voltage gain can be measured (c.f. Figure 10a and Figure 10b, respectively). The net MiBo gain is calculated by comparing the MiBo link to a conventional link (where the HNLF is removed).

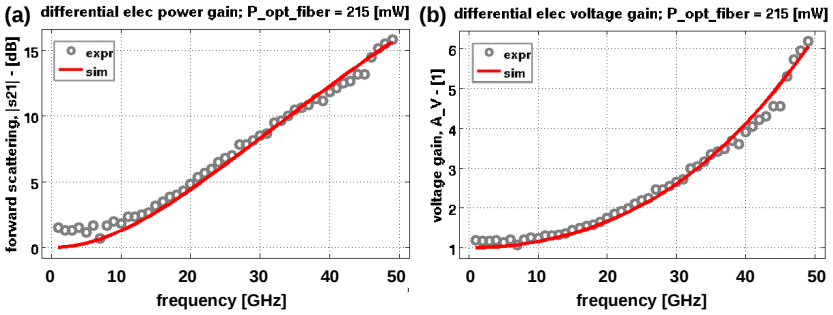


*Figure 10: (a) differential electrical power gain. Note that for the same input RF power, MiBo produces 15 dB more output RF power than the conventional link. (b) This translates to a more than 5-fold reduction in the effective at 50 GHz.*

Note that the experimental gain shape (gray circles) agrees strongly with the simulated side-band only amplification spectrum (red line). Here, MiBo is boosting RF signals by 15 dB at 50 GHz

compared with the conventional link (c.f. Figure 10a), corresponding to a better than 5-fold reduction in the half-wave voltage, $V_\pi$ (c.f. Figure 10b).

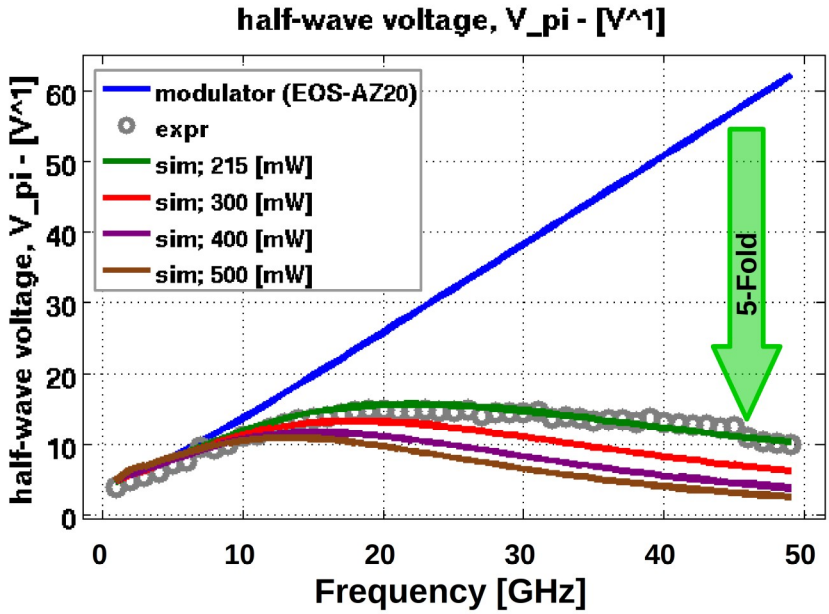


*Figure 11: Effective half-wave voltage for the unboosted (blue) and boosted cases. Experimental measurements (gray) and simulated values (green) show strong agreement in extending the 15 GHz modulator to beyond 50 GHz, and lowering the by more than 5-fold.*

The effective $V_\pi$ frequency response can be is plotted in Figure 11 and compared with the conventional electro-optic $V_\pi$ . Note that where the conventional modulator's 3 dB point is where the $V_\pi$ increases by a factor of 4, at ~15 GHz. This is as expected for the 20 GHz EOSpace AZ-1x2-0K1-20-PFU-SFU. However, the boosted modulator does not cross the 3 dB point, and the 3 dB bandwidth is therefore extended beyond 50 GHz, more than tripling the modulator's effective bandwidth. Simulations show that by increasing the average carrier power to 500 mW, the boosting can be further enhanced, enabling a $V_\pi$ of 3 V at 50 GHz, corresponding to a 20-fold reduction in required drive voltage.

## 5. Experimental Demonstration of Sub-Octave Linearity

In this chapter, the third-order spur-free dynamic range (SFDR) of the MiBo approach is experimentally and numerically measured. Experimental SFDR data is reported at 10 GHz. By utilizing commercial link simulators (VPI transmission maker) with realistic component models simulations at 10 GHz enable predictive SFDR analysis.

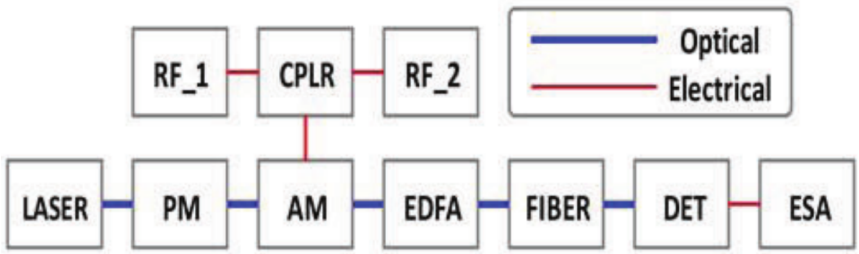


*Figure 12: Experimental and Numerical setup. LASER; PM: phase modulator; AM: amplitude modulator; CPLR: RF coupler; RF_[#]: RF synthesizer, numeric designator; EDFA: erbium doped fiber amplifier; FIBER; DET: photodetector; ESA: electrical spectrum analyzer.*

The experimental and simulated setup are shown in Figure 12. Simulated components are described by VPI transmission maker's industry-trusted and proven component library. The simulated laser is a 1550 nm DFB laser producing 5 mW output power with a RIN of -165dB/Hz. Simulated laser output is amplified to 235 mW with an EDFA that exhibits a 6dB noise figure. The simulated amplitude modulator has 4.1V $V_\pi$ and the -3.0 dB point of the $|S_{21}(f)|$ data is set to be at 15 GHz. The insertion loss of the modulator is set to be 5.5 dB. The 2 km highly nonlinear fiber is modeled using the nonlinear Schroedinger equation [6] with the following coefficients: $\alpha = 1[dB/km]$, $\beta_2 = -10.9[ps^2/km]$, $\beta_3 = 0.062[ps^3/km]$, and $\gamma = 11.6[1/W \cdot km]$. Simulations use a 15 GHz photodetector with 0.70 A/W responsivity and set the optical power input at the detector to +13 dBm. We use ideal RF synthesizers, RF couplers, ESA and other ideal components.

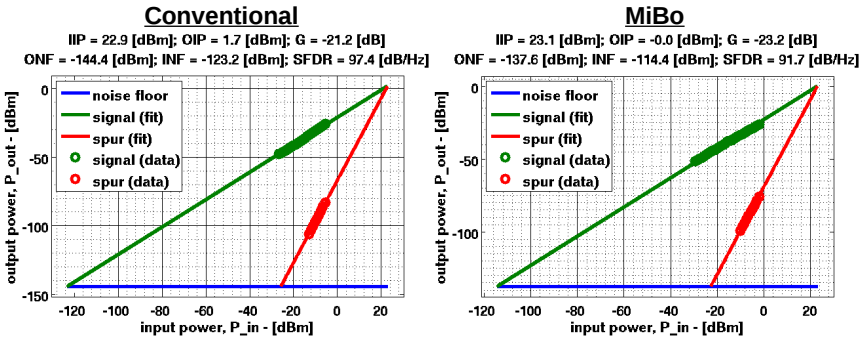


*Figure 13: Experimental SFDR data from a conventional link (left) and a MiBo link (right).*

Figure 13 plots experimental and simulated SFDR. Here, "conventional" denotes a link described by Figure 12 where the phase modulator, EDFA, and fiber have been removed from the link. The SFDR plots are generated using equal power 9.89 and 10.11 GHz tones from RF_1 and RF_2, respectively (c.f. Figure 12). The input tone power is swept in steps, and the power produced at the fundamental and intermodulation frequencies are measured using the ESA. An equivalent noise bandwidth of 1 Hz is utilized throughout. The fits are plotted from the noise floor to the intercept point with slope 1 and 3, respectively. Experimental comparison of the MiBo link to the conventional link shows a 2 dB change in gain and a 6.8 dB increase in the output noise floor due to the EDFA. The increase in the noise floor causes a 8.8 dB reduction in the minimum detectable signal MDS and a 5.7 dB decrease in the $SFDR_3$. Aside from the slight increase in noise floor due to the EDFA, these experiments critically show that MiBo preserves $SFDR_3$, and is therefore well suited to sub-octave links.

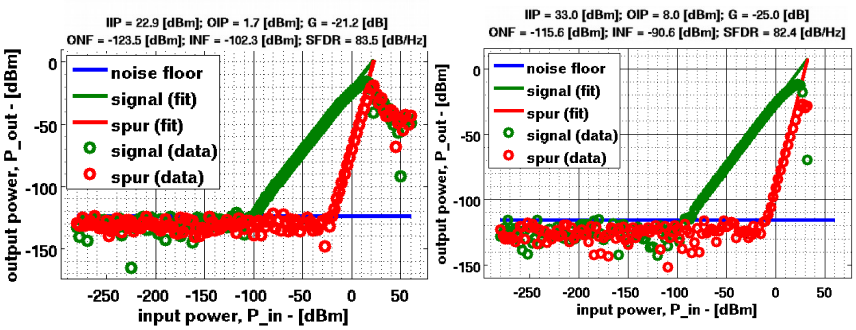


*Figure 14: Simulated SFDR data from a conventional link (left) and a MiBo link (right).*

The simulations confirm the experimental behavior. In the simulations the noise floor rises due to the EDFA and the gain is changed slightly for 10 GHz RF signals. Importantly, both experiments and simulations confirm the ability of MiBo to maintain linearity for sub-octave systems. In summary, these results show that the MiBo approach may offer welcomed relief in high frequency applications where RF powers are limited and optical components suffer from linearity.

# 6. Advanced Simulations

In past chapters, some simplistic simulations based on ideal models of components were performed for proof of principle simulations. Additionally, simulations were performed using the simulation tool VPI, utilized primarily for the transmission of digital optical signals.

In this chapter, sophisticated numerical experiments are used to investigate performance of MiBo and conventional optical links based upon commercially available components and their specifications. Rather than utilize idealized models, this chapter develops models based upon specific commercially available components. These component models are integrated into a full link model where the link is subjected to detailed link analysis. These simulation yield important insights into the minimum detectable signal of the MiBo system versus the conventional system. Critically, the simulated performances have the potential to be realized experimentally, based upon their derivation from commercially available components.

## 6.1. Component Models

The following data is taken from current commercial offerings of various components. The exact manufacturer is not as relevant as the performance that is claimed and offered by existing companies offering state-of-the-art products. Moreover, the author does not wish to make any claims in favor of one particular component over another. Therefore, component manufacturers have been made anonymous.

### 6.1.1. Laser

The laser is modeled after using the following RIN performance. The relative intensity is the power spectral density of the auto-correlation of the laser's time-domain waveform. To

generate a time domain waveform suitable for simulation the specified RIN is first fit to the analytical form of the relaxation oscillation originated RIN.

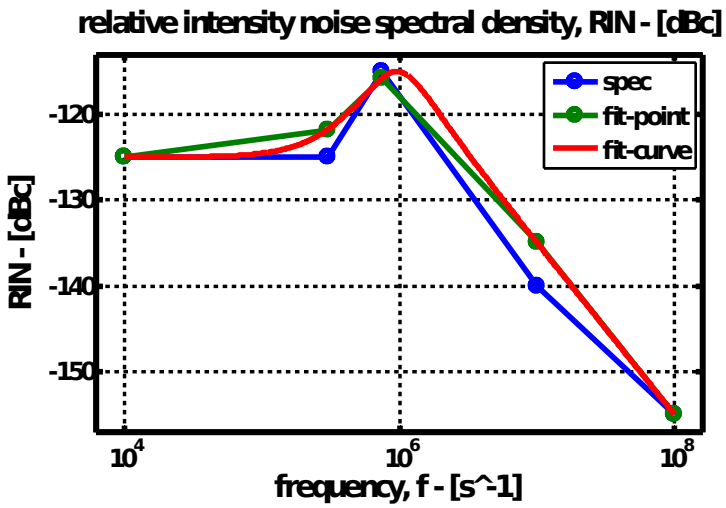


*Figure 15: RIN specification (blue), fitted to the analytical expression for relaxation oscillation based RIN (red), and the minor deviations from the specification (green). Note that the analytical solution allows for frequency extension beyond the specified frequency region.*

Next, a time domain laser waveform with a random noise vector is initialized. The RIN of this laser waveform is calculated, and compared with the fitted analytical RIN formulation. The noise vector is successively modified until the waveform's RIN is numerically equivalent to the analytical RIN spectrum. Note that this allows for RIN extrapolation out to higher, frequencies. The generated time domain laser waveform is below.

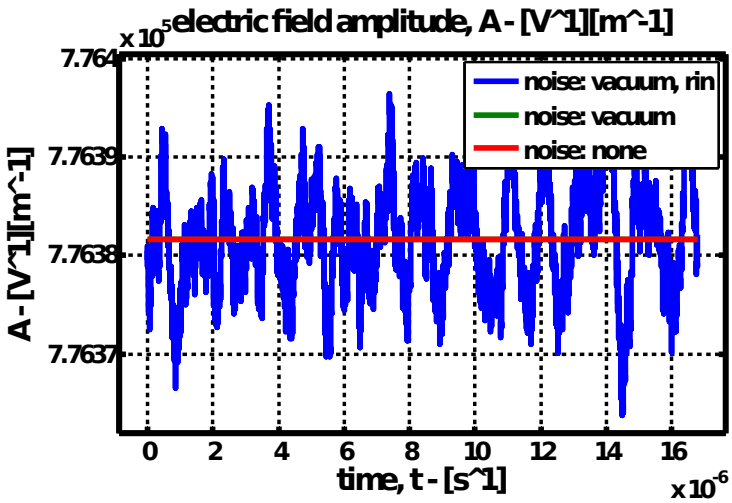


*Figure 16: The time domain waveform of a laser with actual RIN as specified previously (blue). Compare this signal to an idealized laser (red) and a laser with vacuum optical noise (green). Visually the reader can note that the dominant frequency or periodicity of RIN is circa 1 MHz, as would be expected based on the previously specified RIN spectra.*

### 6.1.2. Electrooptic Modulator

The electrooptic modulator is modeled after the following specification. The $S_{21}$ transfer function is scraped from a spec sheet. Once digitized, the data is fit to a general LTI transfer function. The simulation module implements these features by first applying the transfer function of the below modulator to any incoming data, and then modulating an ideal modulator. In this way, bot the frequency response, and cosine transfer function are accounted for. The modulator has a 4.1 volt $V_{\pi}$ at 1 GHz.

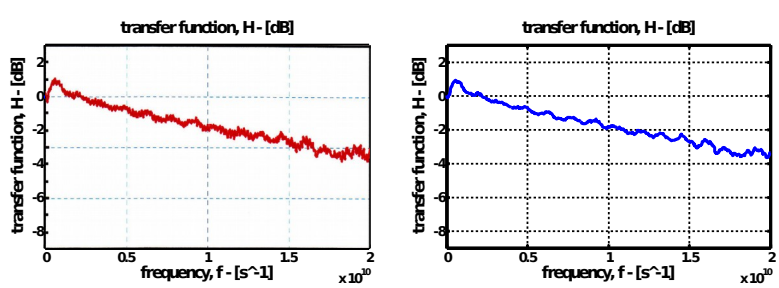


*Figure 17: Specified and digitized modulator frequency response.*

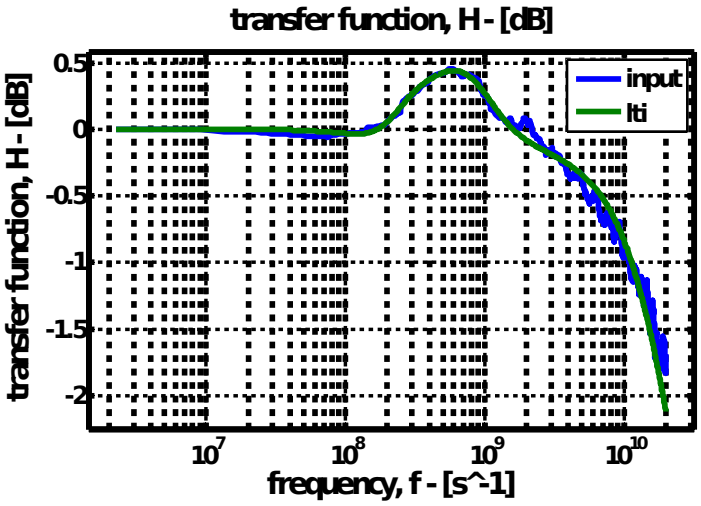


*Figure 18: Ditigitzed modulator data fit to the LTI transfer function, plotted with a logarithmic frequency axis.*

### 6.1.3. Erbium Doped Fiber Amplifier

The erbium doped fiber amplifier (EDFA) is modeled as an ideal amplifier providing preset tunable gain with output powers between 0.5 and 5 watts for input powers between 0 to +3 dBm. The EDFA has an excess noise figure of 6 dB. Both the noise and amplification are frequency banded between 1540 and 1570 nanometers, and act as an ideal passband outside of these frequencies. The noise figure is implemented by initializing a second optical link which contains noise-free ideal components. This link can be referred to as the “ideal” link. The SNR of the optical signal input to the EDFA (with laser noise) is defined by comparison to the ideal link with the noisy link. The ideal optical link includes an analogous noise free EDFA. The SNR of the noisy link’s signal can then be calculated by comparison to the ideal link. Frequency banded Poissonian noise is iteratively added to the noisy link's EDFA output until the EDFA achieves a 6 dB excess noise figure. Below the simulated spectra of a laser passing through this edfa is plotted.

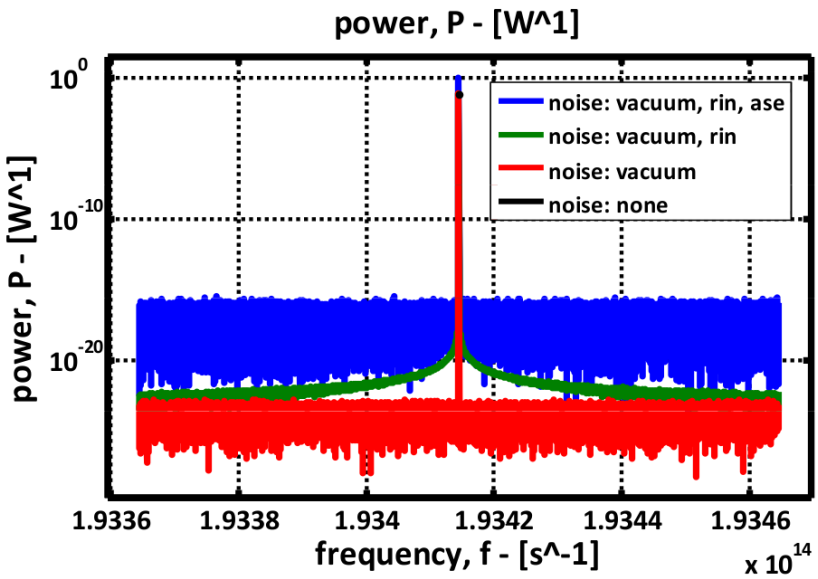


*Figure 19: Simulated OSA trace over a broad frequency range, showing an idealized laser (black), an idealized laser with vacuum noise (red), a commercially available laser with RIN (green), and a commercially available laser amplified by a commercially available EDFA (blue).*

### 6.1.4. Booster

The boosting is accomplished in a $\chi^{(3)}$ nonlinear element. In the case of MiBo the nonlinear element is a highly nonlinear fiber. The physics of this interaction is well described by the nonlinear Schroedinger equation described in previous sections. The same component specifications for the HNLF used previously are used here. A custom split-step Fourier method solver was written. The solver is evaluated by launching input signals that have known analytical expressions that govern their evolution. This includes simple expressions governing optical loss, chirp-free dispersion, chirped dispersion, and lowest order soliton propagation. The results of these tests are below.

The analytical loss test generated no plots. Suffice it to say that the optical power decreased as expected according the $\alpha$ parameter. The dispersion test utilized a short pulse with no chirp. Dispersive pulse broadening was witness according to analytical expressions.

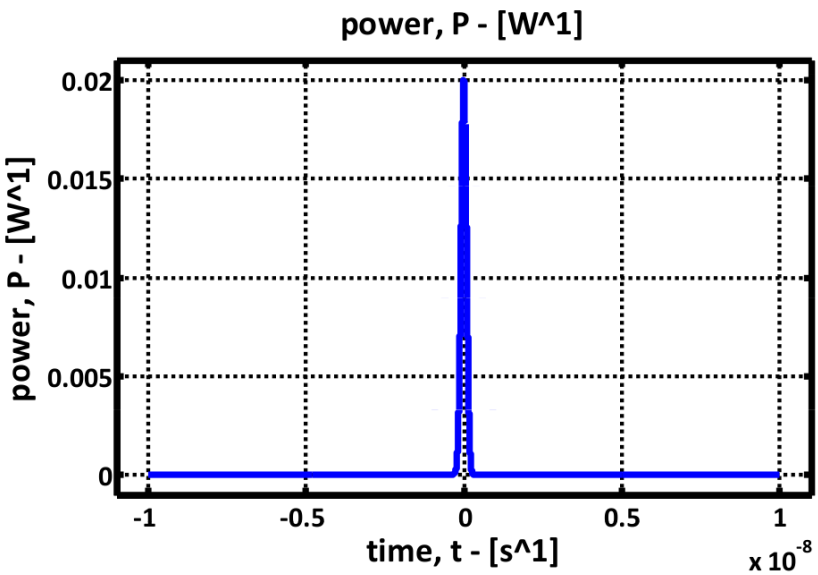


*Figure 20: A short pulse before dispersion which yielded analytical dispersion as a function of propagation distance.*

The dispersion of chirped pulses was simulated, and was shown to reproduce the familiar family of curves from [6], as shown below.

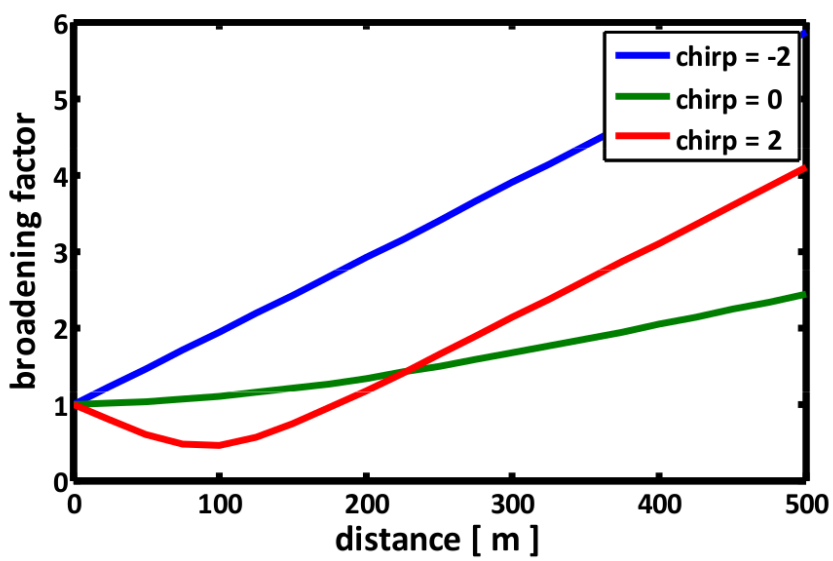


*Figure 21: Broadening factor as a function of distance for pulses with various chirp.*

Finally, an analytical soliton was launched into a fiber with the exact power as required for soliton propagation per the fiber's dispersion and nonlinearity. The exiting pulse was as expected, an exact match in the temporal domain (see below).

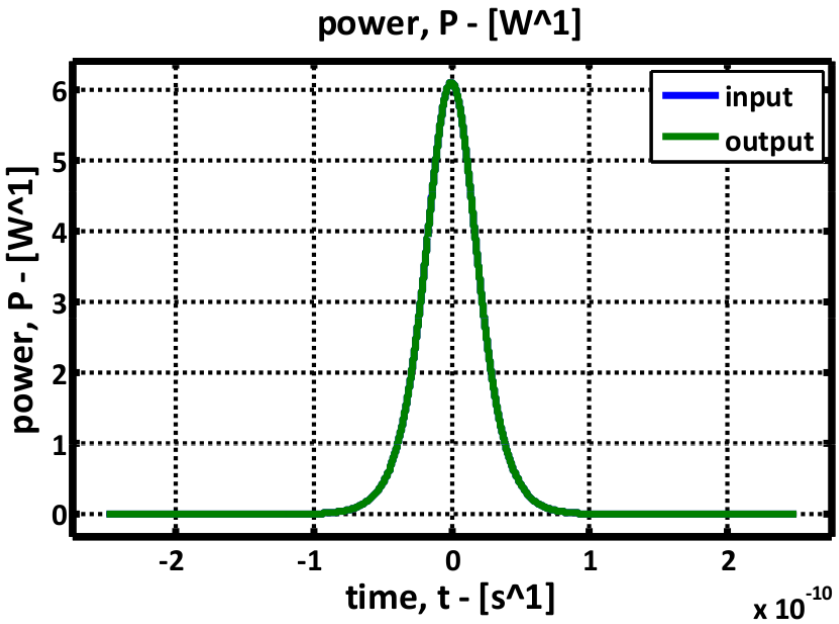


*Figure 22: The temporal input and output of a soliton after propagating through 500 meters of fiber. Note that the input and output are exactly identical. If the nonlinear parameter is zeroed, the input will rapidly disperse at the output, as would be expected. The Booster model therefore captures the desired nonlinear, lossy, and dispersive behavior of commercial fibers.*

Therefore, the component model for commercial highly nonlinear fibers can accurately represent loss, dispersion, and nonlinearity for complex input waveforms.

### 6.1.5. Photodiode

The photodiode is modeled after a commercially available 50 GHz photodiode. The photodiode response has a 3 dB roll off at 50 GHz. The maximum recommended input power is 10 dBm, responsivity is 0.5 A/W, and the dark current is 200 nA.

The frequency response is modeled by extracting the measured $S_{21}$ response from the part's data sheet, and fitting it to an LTI transfer function. The model will accept incoming time

domain signals, and pass them through the modeled LTI system, before performing ideal photodetection with respect to frequency. In this way, the frequency response of the photodiode is managed.

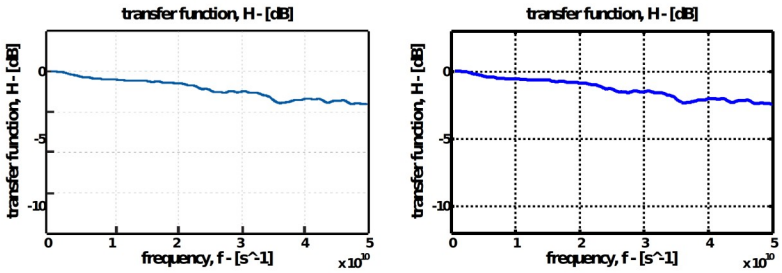


*Figure 23: Commercially available photodiode's frequency response, from manufacturer (left), and digitized copy of the same frequency response (right).*

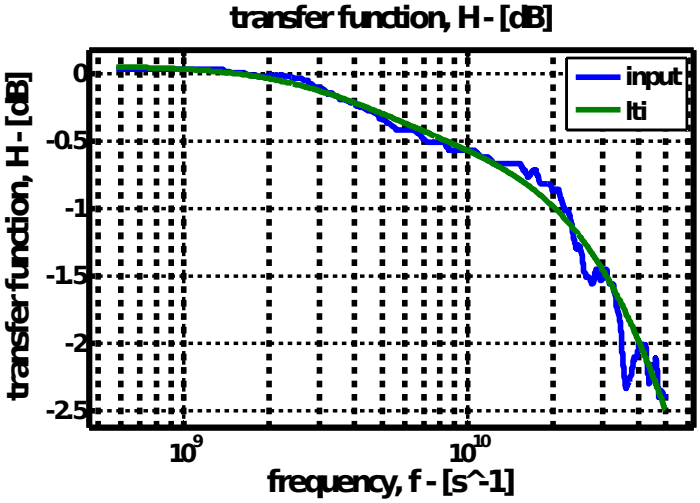


*Figure 24: Digitized photodiode frequency response plotted with a logarithmic x-axis, and overlaid LTI response. This LTI response carefully models the true frequency response of this commercial photodiode.*

Saturation and compression of the photodiode are critical sources of nonlinear distortion in analog optical links. Therefore these features must be included in the simulations. Photodiode saturation data is extracted from the manufacturers specification sheet. A laser is modulated at 10 GHz and input into a variable optical attenuator before entering the photodiode under test. The provided data shows the electrical power generated at 10 GHz as a function of optical input power. Saturation is therefore modeled as a reduction of responsivity as a function of input

optical power. Note that the linear portion of the curve represents a constant responsivity, given at a frequency of 0 Hz to be 0.5 A/W. The responsivity is reduced as the laser power is increased. The convolution of responsivity and frequency response will therefore produce the full experimental behavior.

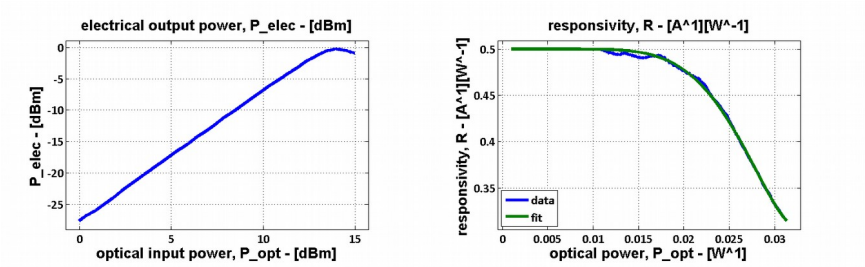


*Figure 25: Photodiode saturation is extracted from specification sheet. Provided data shows the electrical power generated at 10 GHz as a function of optical input power for a 10 GHz analog modulated laser (left). Saturation is therefore modeled as a reduction of responsivity as a function of input optical power (right). The convolution of responsivity and frequency response will therefore produce the correct experimental behavior.*

The photodiode is the first component in an analog optical system where a host of important noise sources either originate or become manifest. The photodiode itself is responsible for the introduction of thermal noise and shot noise. In addition, relative intensity noise (RIN) generated by the laser and amplified spontaneous emission noise (ASE) generated by the EDFA are both witnessed at the photodiode. These sources of noise increase the links overall noise figure (NF), and reduce the link's signal to noise ration (SNR). Below is a table showing the various noises and their impact on noise power and signal to noise ratio as a function of optical power input to the photodiode.

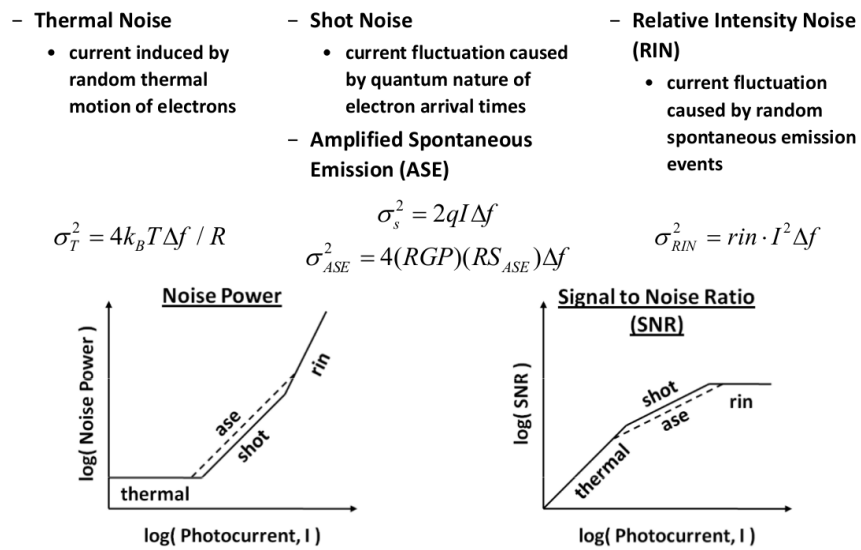


*Figure 26: Noise phenomena generated and manifest in the photodiode's signal.*

Both thermal and shot noise are implemented in the photodiode model according to the expressions above. ASE and RIN will both become manifest during detection, depending on their dominance and the incidence of RIN before photodiode damage. Below the SNR is plotted as a function of photodiode incident optical power. Witnessed is the thermal SNR scaling, shot noise SNR scaling, and damage onset.

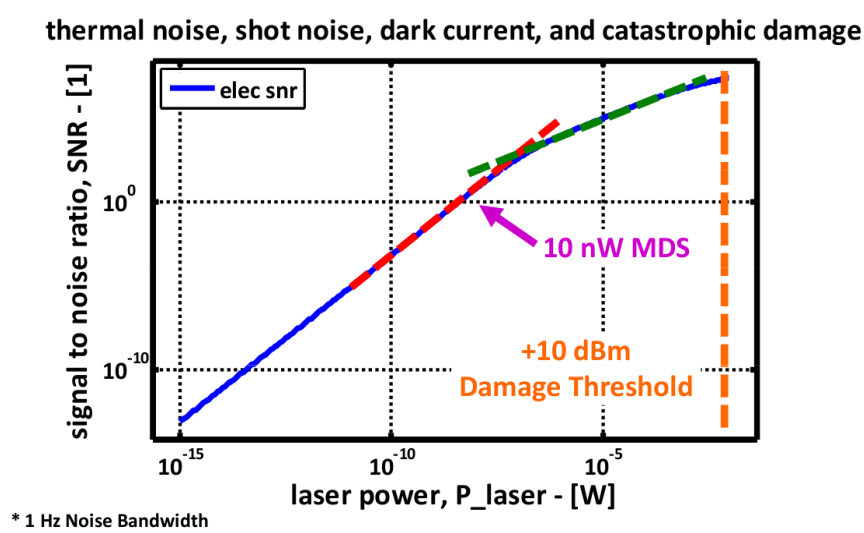


*Figure 27: Photodiode model exhibiting thermal noise, shot noise, and catastrophic damage.*

## 6.2. MiBo System Models

This section incorporates the component models described above into system link models. The systems are simulated to determine the conventional and MiBo: frequency response, spur-free dynamic range (SFDR), and minimum detectable signal (MDS) which is used to quantify system sensitivity. The system schematic for these links is the same as described in previous sections.

The gain spectrum is determined by sweeping the frequency of the signal generator with a fixed power and detecting the output signal power at the photodiode using an electrical spectrum analyzer. By comparing the input electrical power and the output electrical power as a function of swept frequency, the frequency response can be measured. Below we see the frequency response of a conventional optical link using the above described components, and a MiBo link using the above described components. Note that the gain shows 8 dB flatness in the MiBo case over 150 GHz, where the conventional link shows 55 dB rolloff over 150 GHz.

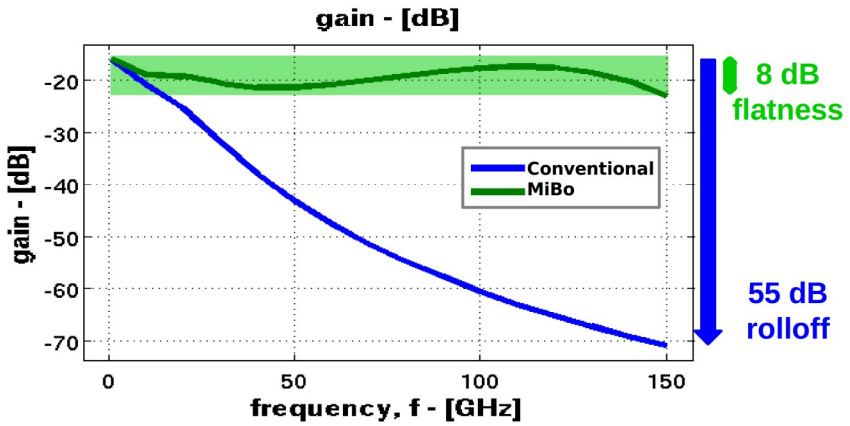


*Figure 28: Comparison of gain for MiBo and conventional links. The MiBo link shows 8 dB flatness over 150 GHz whereas the conventional link shows 55 dB rolloff.*

The SFDR can be analyzed as a function of frequency. The SFDR is first determined at a single frequency by successively increasing the power of two synthesizers in lock-step, both of

which are connected to the conventional electrooptic modulator, followed by measuring the resulting spectra on the electrical spectrum analyzer. The SFDR is the range of input powers between which the signal first eminates out of the noise floor, and the intermodulation spur first eminates out of the noise floor. In this range, the signal is ever present, and the intermodulation distortion is always absent. Hence the name, spur-free dynamic range. The SFDR as a function of frequency can be found by sweeping the two synthesizer frequencies $f_{low}$ and $f_{high}$ where $f_{center}=f_{low}+f_{span}/2=f_{high}-f_{span}/2$ and $f_{span}=0.025\times f_{center}$ . The resulting SFDR as a function of frequency is below.

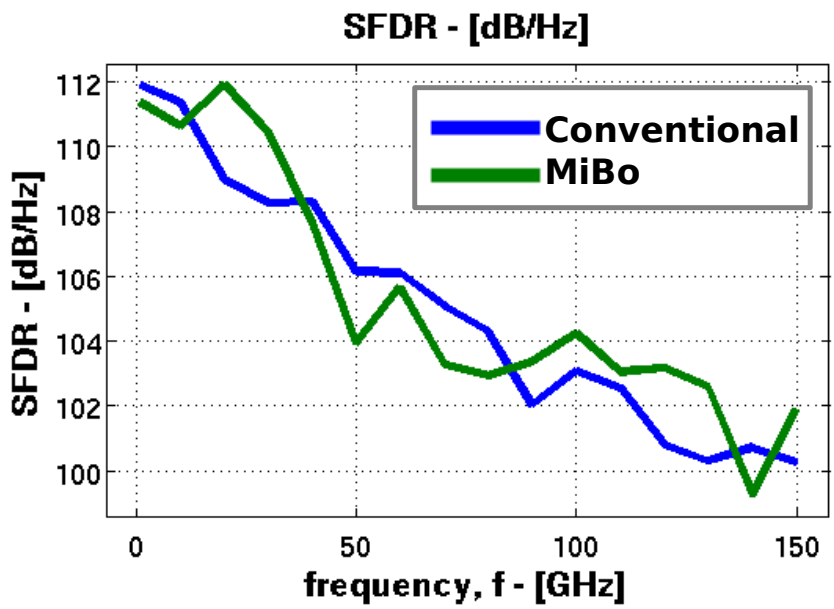


*Figure 29: The SFDR as a function of center frequency is plotted for both the conventional and MiBo links. Note that both systems have the same SFDR.*

Note that the SFDR is essentially equivalent between the conventional and MiBo systems. In both cases the SFDR is approximately 112 dB/Hz$^{2/3}$ at DC and 100 dB/Hz$^{2/3}$ at 150 GHz.

It's possible to plot the linear operating region as the MDS to the MDS + SFDR, as shown below. In other words, the linear operating region is bounded on the lower end by the minimum

detectable signal, and on the upper end is bounded by the minimum detectable signal plus the SFDR (at which point distortion becomes manifest).

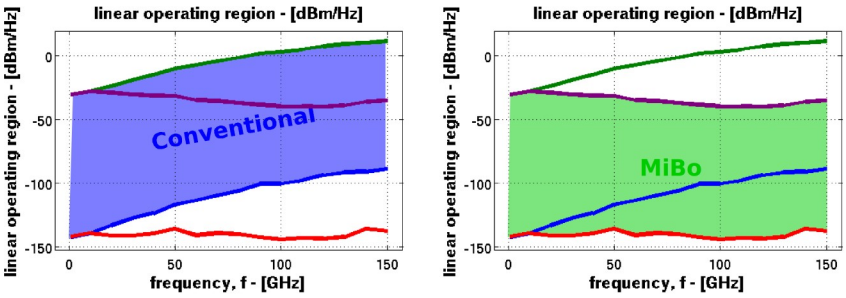


*Figure 30: Linear operating range as a function of frequency. Note that the conventional link has the same SFDR, but that the range is less sensitive, or requires larger input powers to achive the same SNR.*

Now that it's clear that the overall usable dynamic range is equivalent for the MiBo and the conventional case, it is possible to investigate the minimum detectable signal (MDS). The MDS is the input power for which the output signal has an SNR of 1. This data is generated in the process of creating the SFDR data, i.e. it is the intercept of the fundamental with the noise floor is the MDS.

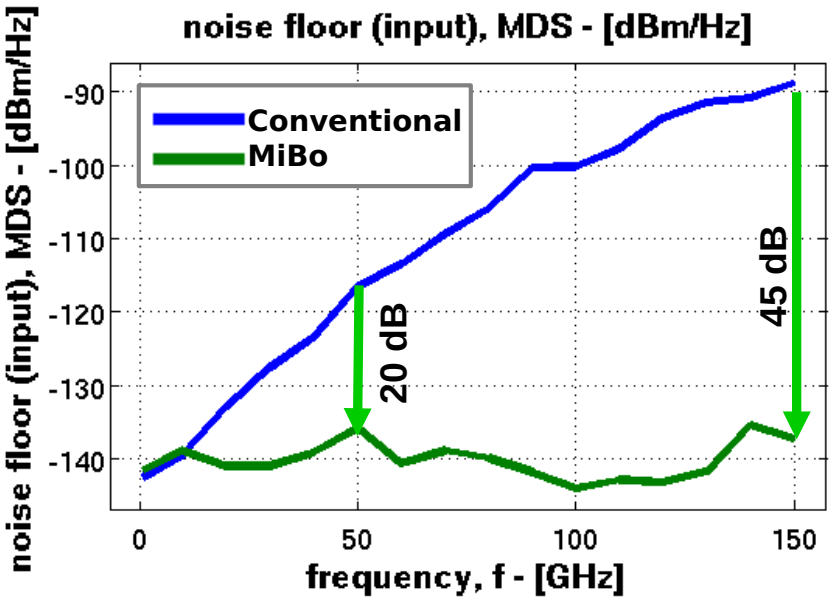


*Figure 31: The minimum detectable signal (MDS) as a function of frequency. Note that MiBo is 20 dB more sensitive than the conventional link at 50 GHz, and 45 dB more sensitive at 150 GHz.*

Above we see that MiBo is 20 dB more sensitive than the conventional link at 50 GHz, and 45 dB more sensitive at 150 GHz.

7. Phase Modulation

MiBo is primarily designed for use with intensity modulated analog optical links, however methods to boost phase modulation were also investigated. In the case of phase modulated signals, the phase modulation can be converted to intensity modulation by use of a dispersive fiber.

| Dispersion Specifications | |
|---|---|
| Dispersion @ 1550 nm | -49.00 to -30.00 ps/nm*km |
| Dispersion Slope @ 1550 nm | -0.155 to -0.075 ps/nm$^2$*km |
| Typical Effective Area | ≥26.8 μm$^2$ |
| Polarization Mode Dispersion | ≤0.05 ps//km |

2km DCF

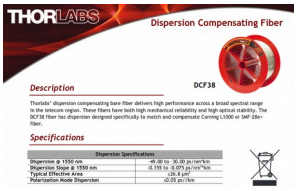


*Figure 32: Specifications of commercially available DCF used in simulations.*

Below is a simulation where a 50 GHz phase modulated signal is dispersed using 2 km of th above described commercially available DCF fiber. The resultant was the phase modulation was converted into amplitude modulation. Next, the signal was input into the same boosting fiber, where the modulation strength was increased considerably by the MiBo process. This preliminary exploration shows the potential of this exciting area for further investigation.

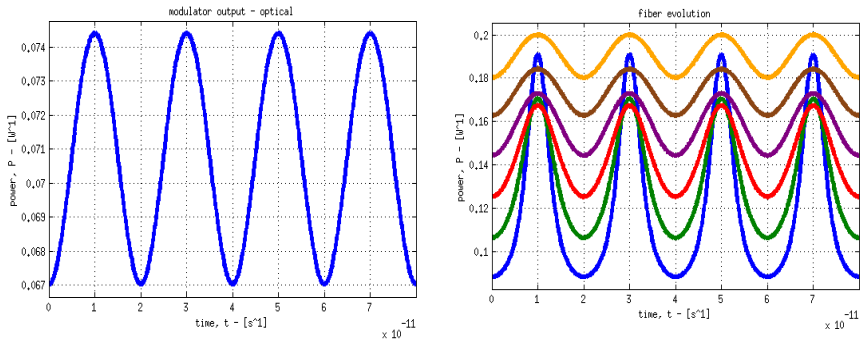


*Figure 33: Amplitude fluctuation of signal after dispersion (left). The amplitude strength increases as a function of propagation down the HNLF from the point of launching (yellow) to the end of the 2 km fiber (blue). More or less boosting can be obtain by choosing the desired length of fiber.*

## 8. MiBo prototype

A MiBo prototype was developed following initial experiments so the MiBo approach could be tested in application environments and so that state-of-the art commercial components could be utilized to test the approach's performance. Following simulations presented in previous chapters, it was clear that state-of-the-art components similar to those simulated could improve MiBo's performance. Below is the first generation MiBo system setup.

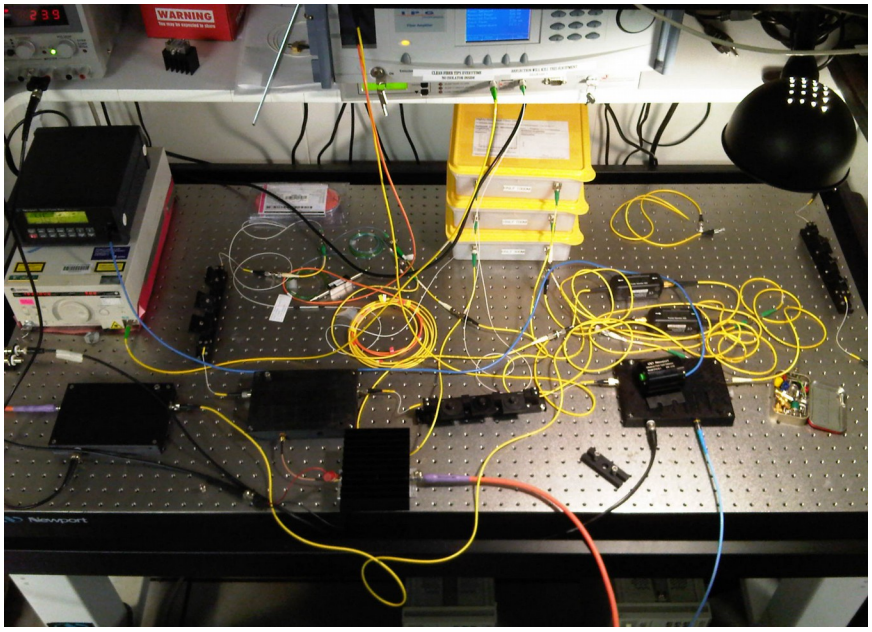


*Figure 34: MiBo system. The system required a 6 foot by 4 foot optical breadboard and a full shelf of equipment.*

The various components used in the MiBo system required a full 6 foot by 4 foot optical table as well as an entire storage shelf.

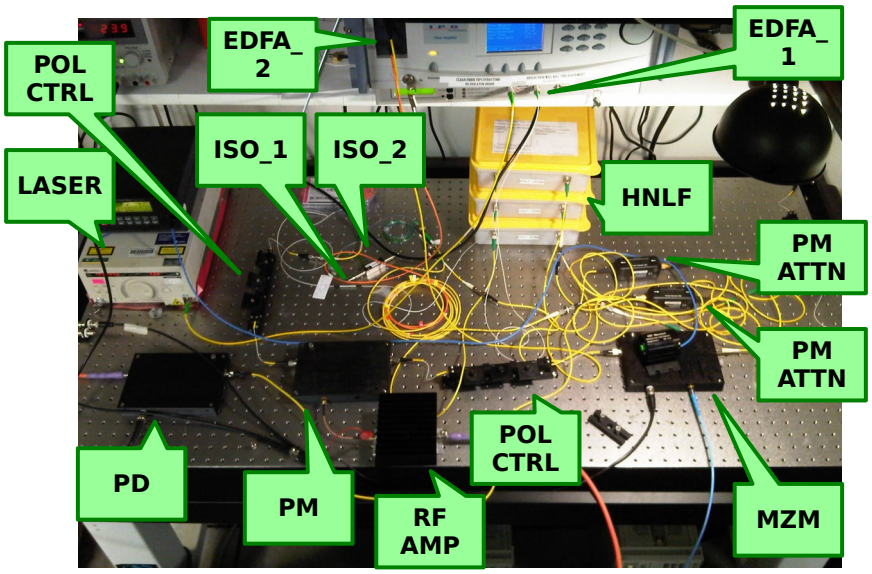


*Figure 35: MiBo system with individual components called out.*

If the size of the MiBo system could be reduced, then in-field application development could begin. In this way, MiBo could be used as a drag and drop replacement system for application development. The system consists of a 1600 km piece of HNLF fiber cut from the same spool as mentioned in previous sections. An OEM EDFA from Amonics was used to provide up to 2 W of output power. The laser was a NKT Koheras Boostik C15 low RIN laser with 100 mW output. The photodiode was a Finisar 50 GHz xpdv2150r. The AWG was an OEM integrated AWG from Wavepond which drove a 500 MHz Minicircuits ZHL-1-2W amplifier, which fed a EOspace polarized phase modulator. The amplitude modulator was an EOspace AZ-DV5-40-PFU-SFU-SLB65 MZM have a 4.2V half-wave voltage, a 35 GHz 3dB point, and a flat frequency response out to 65 GHz. Below is the prototype design and interface specifications.

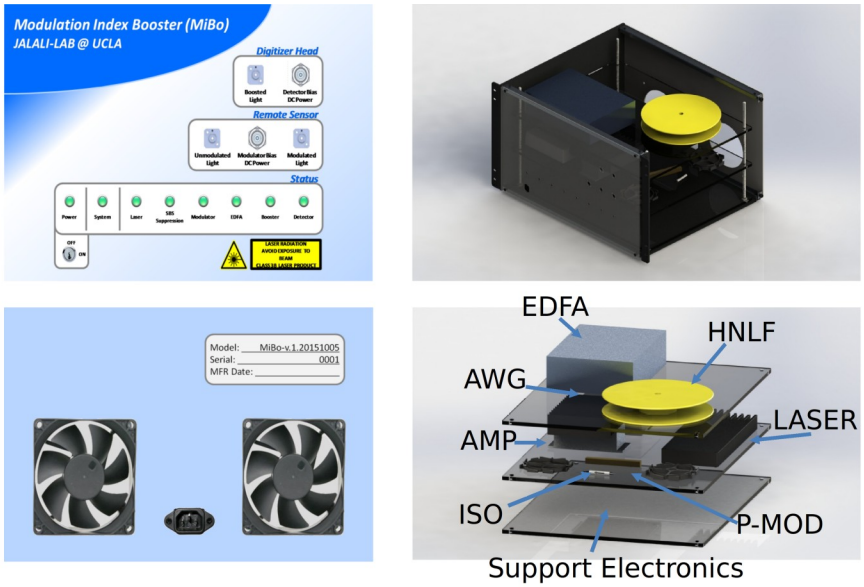


*Figure 36: Design of MiBo prototype. A 4U 19 inch rackmount module is designed to contain all MiBo components. The MiBo unit directly interfaces with a remote sensor or modulation unit, and a photodiode or digitizer head. A single turnkey operates the unit.*

Below is an image of the MiBo prototype as realized. The unit is essentially the same as designed, containing all components necessary to achieve modulation index boosting and sensitivity enhancement.

*Figure 37: Realized MiBo prototype. The prototype contains state-of-the-art components as necessary to achieve sensitivity enhancement.*

The MiBo prototype was tested using the same methodology previously described. The frequency response was measured by sweeping the frequency of the synthesizer and measuring the resulting spectrum using the electrical spectrum analyzer. As expected the second generation system provided essentially the same boosting, achieving more than 13 dB of boosting at 50 GHz for the same input booster power (200 mW).

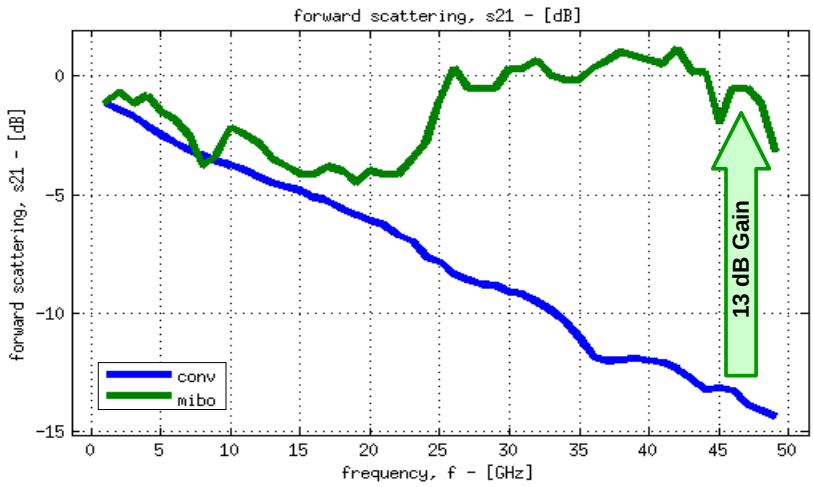


*Figure 38: Experimental frequency response of MiBo versus conventional link. Note that MiBo boosts signals by as much as 13 dB at 50 GHz.*

By comparing the frequency response of the MiBo link to that of the conventional link, the gain provided by MiBo can be calculated, as plotted below.

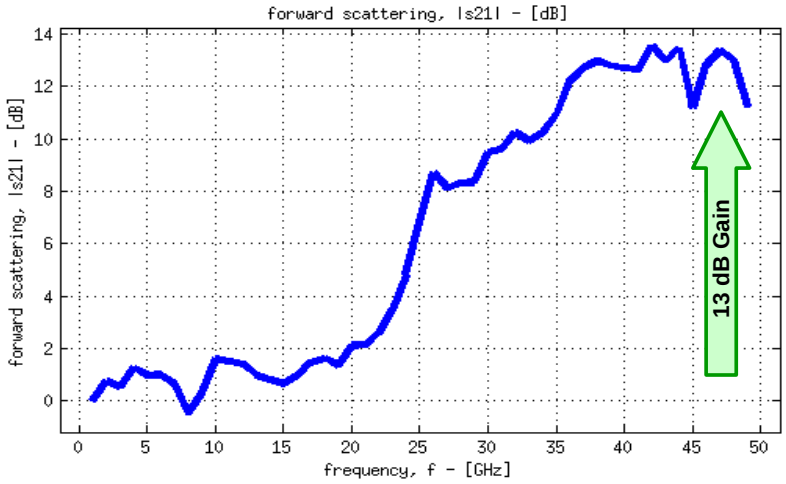


*Figure 39: MiBo provides as much as 13 dB gain at 50 GHz.*

Note the rapid increase in gain in Figure 39 circa 25 GHz. This is an exciting area for further investigation. This may be caused by small signal perturbations as governed by the nonlinear Schroedinger equation, or additional dynamics which may reveal new insights. The effective half-wave voltage is plotted below. Here MiBo achieves an effective half-wave voltage of approximately 4 volts at 50 GHz, and an overall 5-fold reduction in the effective half-wave voltage.

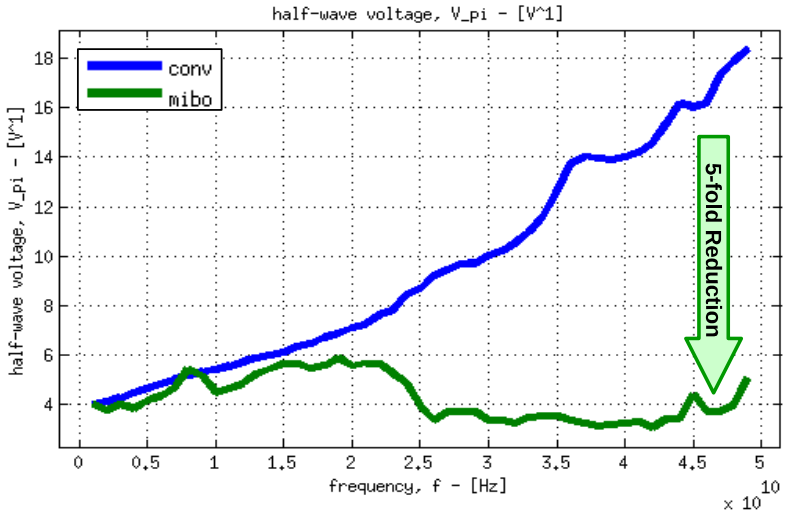


*Figure 40: Experimental data showing the effective half-wave voltage of the MiBo link and conventional link as a function of frequency.*

Additionally the SFDR of the conventional and MiBo links were measured at 20 GHz, as plotted below. The SFDR of the MiBo link was measured as 102.9 dB/Hz$^{2/3}$ compared with 105.1 dB/Hz$^{2/3}$ for the conventional link, showing that MiBo preserves SFDR.

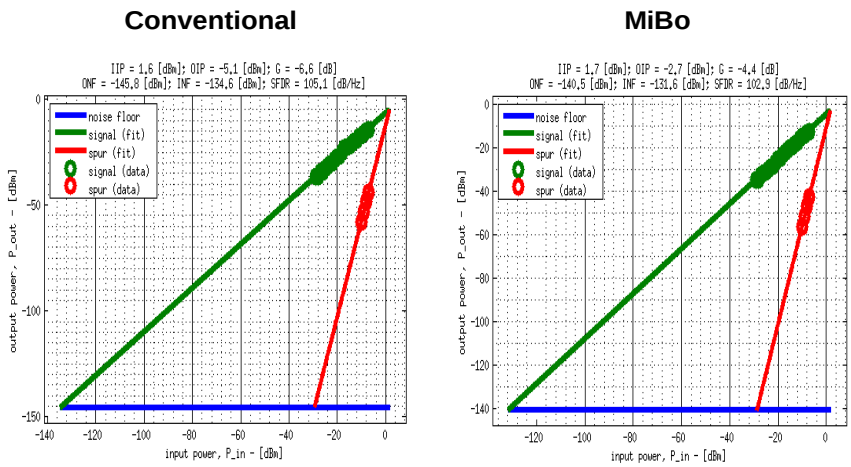


*Figure 41: Experimental SFDR of conventional and MiBo link at 20 GHz.*

## 9. Time-Stretch MiBo

MiBo is compatible with all-optical modulation, followed by time-stretch digitization. This scheme, known as Time-Stretch MiBo, aims to achieve record digitization bandwidths, upwards of 150 GHz, with revolutionary sensitivity (MDS). The system involves a MiBo stage at the front-end, followed by an all-optical modulator that employs a chirped Fourier-Domain Mode Locked Laser (C-FDML) pump, followed by a dispersive fiber. Utilizing this setup, the high-sensitivity of MiBo, and the high-frequency digitization capabilities of time-stretch analog to digital converters (TS-ADCs) and be combined. Critically, 150 GHz digitization can be achieved with 30 GHz digitizer hardware. The concept is outlined below. This is an exciting area of active research, which could be investigated both numerically and experimentally, following the concept outlined in this chapter.

The overall system amplitude response is the overlap between the EO-modulator amplitude response and the Digitizer amplitude response, as shown below. MiBo is capable of both boosting and extending the EO-modulator response, whereas Time-Stretch is capable of extending the Digitizer's amplitude response.

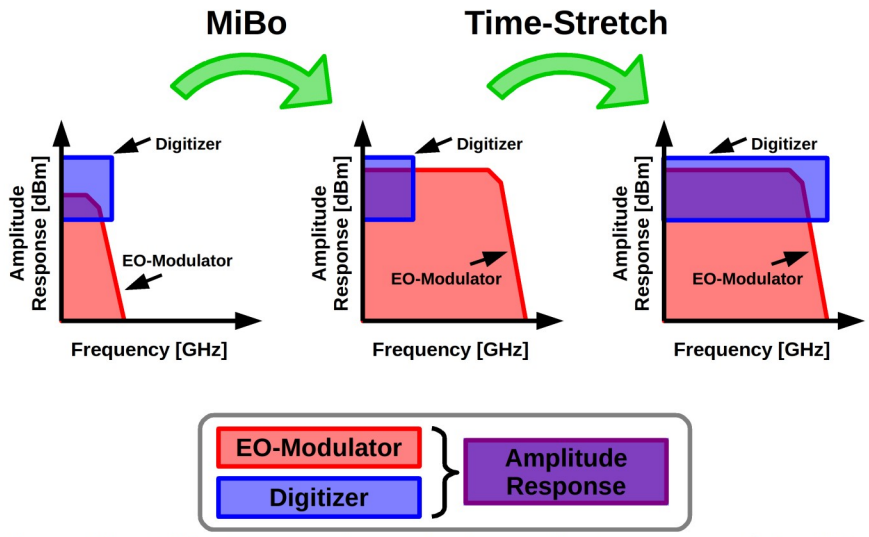


*Figure 42: MiBo boosts and extends the amplitude response of the EO-modulator. Time-Stretch extends the amplitude response of the Digitizer.*

The result is 150 GHz digitization at high-sensitivities using 30 GHz digitizers. This is accomplished as shown below.

The system is shown below. Here we see the signal envelope evolution above each component.

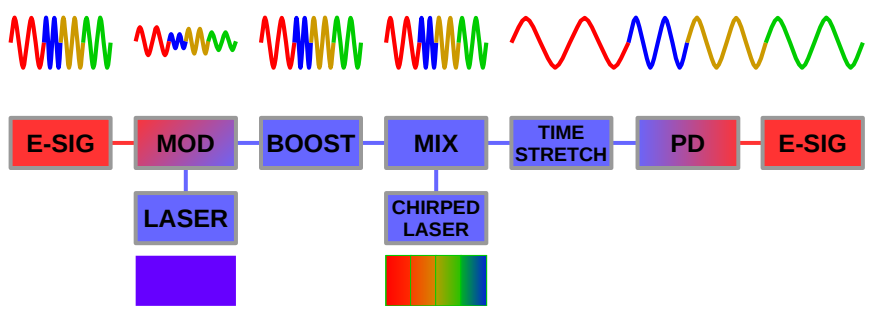


*Figure 43: System diagram for Time-Stretch MiBo concept.*

First a broadband signal enters a modulator. The low frequency electrical signals (red) are attenuated because the $V_\pi$ is too high, and the high frequency electrical signals (blue) are attenuated even more so because the bandwidth rolloff of the modulator is limited to 35 GHz.

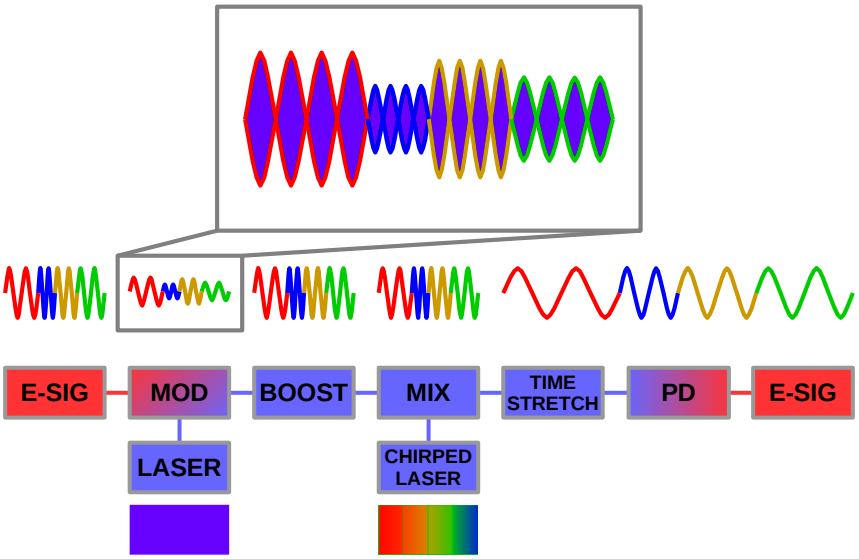


*Figure 44: A CW laser is amplitude modulated by the electrical signal in the EO-Modulator. Note, the electrical signal is broadband, having high-frequency (blue) and low-frequency (red) components. The low frequency electrical signals (red) are attenuated because the* $V_\pi$ *is too high, and the high frequency electrical signals (blue) are attenuated even more so because the bandwidth rolloff of the modulator is limited to 35 GHz.*

In the above figure we see that this envelop signal is imprinted on top of a single-frequency laser, such as a continuous-wave fiber or semiconductor laser. Note that the ~200 THz optical carrier (solid purple) oscillates so rapidly in contrast to the ~150 GHz amplitude modulation from the EO-modulator that the purple ~200 THz signal appears solid. This is just conventional amplitude modulation where the carrier frequency is much higher than the signal frequency. This signal enters the booster and the original broadband signal is restored using the MiBo method described in detail in previous sections. Note that the MiBo booster preferentially boosts the high frequency signals (blue) but also boosts the lower frequencies (red).

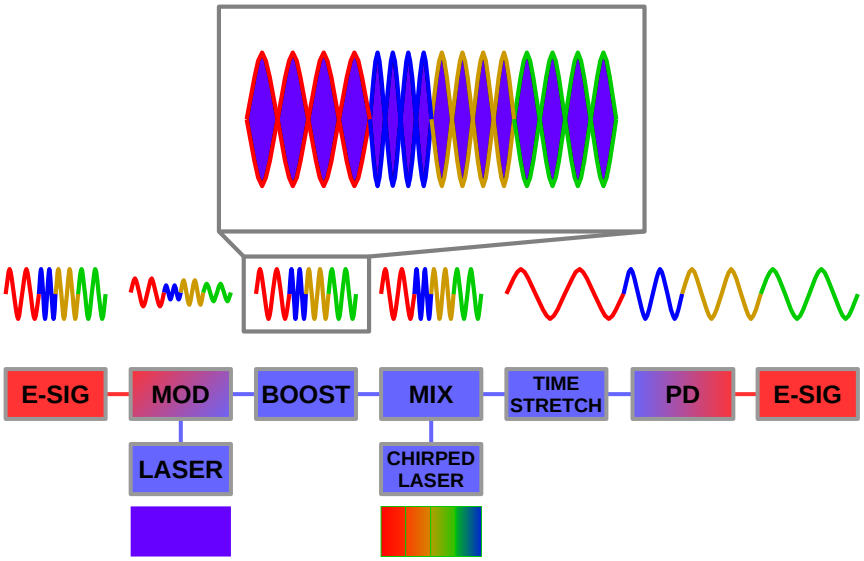


*Figure 45: The MiBo booster restores the broadband signal by boosting all signals and preferentially boosting the high-frequency signals.*

In the next step, the signal is rainbow encoded. Here the signal is comprised of a CW single-frequency optical carrier that has been modulated by a broadband signal. The rainbow encoding of this signal is accomplished in a nonlinear optical mixer using a chirped pump, such as a chirped Fourier-Domain Mode Locked Laser (C-FDML). This rainbow encoding, known as all-optical-modulation, has been successfully demonstrated [33]. Therefore the integration of these two techniques should be theoretically straight forward.

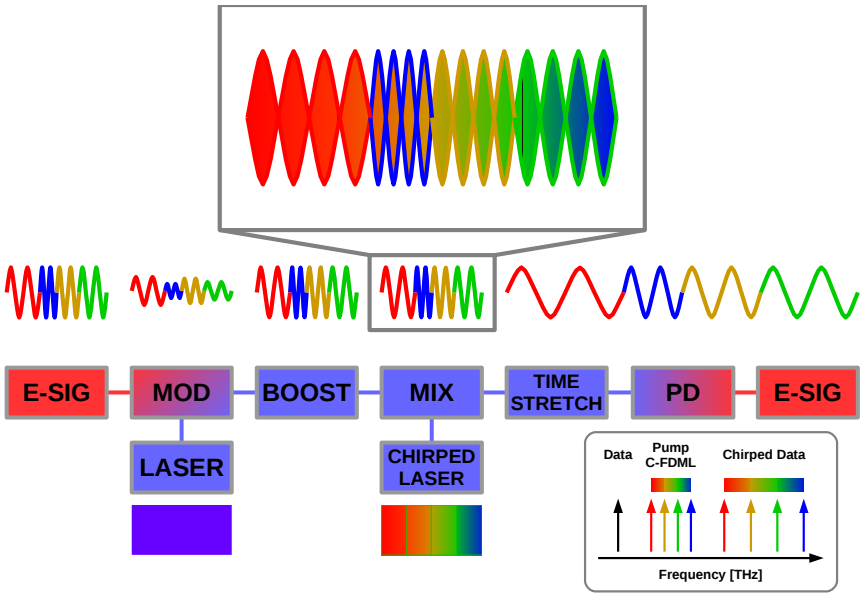


*Figure 46: The signal is rainbow encoded using a C-FDML. Note that the amplitude envelope remains the same, but the optical carrier is now chirped from low optical frequency (solid red) to high optical frequency (solid blue). The lower left inset shows the signal, or "Data" which is relatively narrow band compared with the C-FDML pump and chirped data. The Data signal, emitted from the booster, is input to the mixer with the C-FDML; the two mix together, producing the rainbow encoded chirped data.*

The signal is rainbow encoded using a C-FDML. Note that the amplitude envelope remains the same, but the optical carrier is now chirped from low optical frequency (solid red) to high optical frequency (solid blue). The lower left inset shows the signal, or "Data" which is relatively narrow band compared with the C-FDML pump and chirped data. The "Data" signal which is emitted from the booster is input to the mixer along with the C-FDML; the two mix together, producing the rainbow encoded chirped data. The "Data" signal and C-FDML pump are the filtered out, leaving the chirp data signal only.

Finally, the signal enters a dispersive element where it undergoes Time-Stretching, which uses optical dispersion to slow the very information that is contained in the signal. A Time-Stretch factor of M=5 is sufficient to slow 150 GHz signals so that they can be effectively digitized by a 30 GHz digitizer.

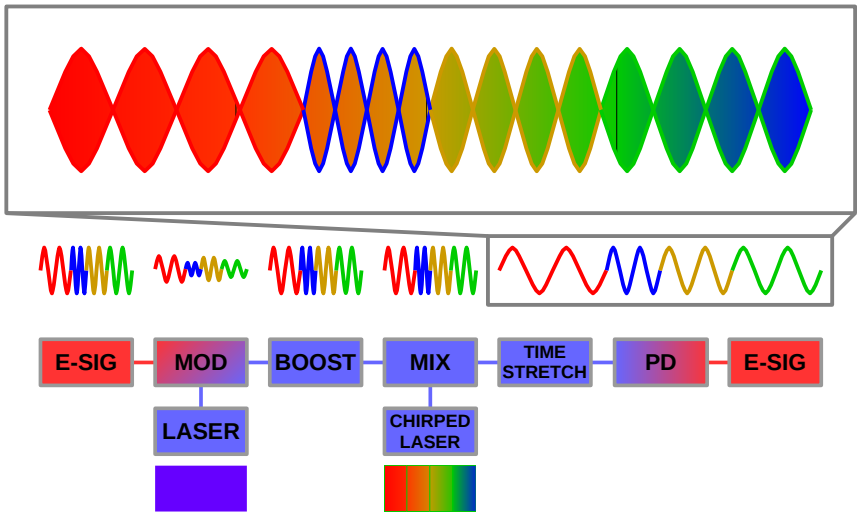


*Illustration 1: The rainbow encoded signal undergoes Time-Stretching, slowing the signal information. Note the envelope has been stretched in time, effectively slowing the very information contained in the signal.*

By joining these two promising technologies, MiBo and Time-Stretch, it is possible to capture low-power non-repetitive single-shot signals with high-sensitivity and bandwidths up to 150 GHz using 30 GHz digitizers.

## 10. Photon Doppler Velocimetry

The purpose of this study is to investigate the potential for performance enhancement by combining two mature techniques, Photon Doppler Velocimetry (PDV), developed by Sandia, and Modulation Index Boosting (MiBo), developed at UCLA in collaboration with Sandia. PDV utilizes Doppler velocimetry to track unconventionally high-velocity objects. In the course of operation, PDV generates high-frequency broadband waveforms with spectral content from 1-70 GHz. MiBo is a technique that preferentially boosts or amplifies high-frequency signals by as much as 15 dB at 50 GHz. MiBo gain extends up to 150 GHz, making the technique especially relevant to PDV. This proof-of-principle study analyzes the expected performance impact of inserting a MiBo module in to a PDV system. The unoptimized results presented here show that MiBo is able to improve PDV detection sensitivity by 10 dB in general, and by as much as 20 dB for challenging Doppler frequency shifts beyond 40 GHz. These results offer a compelling case for further development of MiBo assisted PDV systems.

### 10.1. PDV Waveform Generation

**Doppler Velocimetry**

In Doppler velocimetry a target is irradiated by a monochromatic source with frequency $f_{incident}$. Assume the source and target have a relative velocity difference given by $\Delta v$, where $\Delta v$ is positive for closing distance and negative otherwise. The reflected radiation will be shifted in frequency by $\Delta f$, from $f_{incident}$ to $f_{reflected}$, as described below.

$$\Delta f = \frac{2\Delta v}{c} f_{incident} = f_{reflected} - f_{incident} \tag{9}$$

Solving for $f_{reflected}$ yields the following.

$$f_{reflected} = f_{incident}\left(1 + \frac{2\Delta v}{c}\right) \quad . \tag{10}$$

**Interferometry**

In interferometry suppose there exists two fields, a signal and a local oscillator (LO). The fields are given by,

$$E_{sig}(t) = E_{sig}\cos(\omega_{sig}t + \phi_{sig}) \tag{11}$$

and,

$$E_{lo}(t) = E_{lo}\cos(\omega_{lo}t) \quad . \tag{12}$$

When these two fields are interfered, the optical intensity is proportional to the sum of these two fields squared.

$$\begin{aligned} I &\propto (E_{sig}(t) + E_{lo}(t))^2 \\ &= (E_{sig}\cos(\omega_{sig}t + \phi_{sig}) + E_{lo}\cos(\omega_{lo}t))^2 \\ &= \frac{E_{sig}^2}{2}(1 + \cos(2\omega_{sig}t + 2\phi_{sig})) + \frac{E_{lo}^2}{2}(1 + \cos(2\omega_{lo}t)) \\ &+ E_{sig}E_{lo}[\cos((\omega_{sig} + \omega_{lo})t + \phi_{sig}) + \cos((\omega_{sig} - \omega_{lo})t + \phi_{sig})] \\ &= \underbrace{\frac{E_{sig}^2 + E_{lo}^2}{2}}_{constant\ component} + \underbrace{E_{sig}E_{lo}\cos((\omega_{sig} - \omega_{lo})t + \phi_{sig})}_{beat\ component} \\ &\underbrace{+ \frac{E_{sig}^2}{2}\cos(2\omega_{sig}t + 2\phi_{sig}) + \frac{E_{lo}^2}{2}\cos(2\omega_{lo}t) + E_{sig}E_{lo}\cos((\omega_{sig} + \omega_{lo})t + \phi_{sig})}_{high-frequency\ component} \end{aligned} \tag{13}$$

The high-frequency components are typically removed through filtering. The resulting expression is below.

$$I \propto \underbrace{\frac{E_{sig}^2 + E_{lo}^2}{2}}_{constant\ component} + \underbrace{E_{sig}E_{lo}\cos((\omega_{sig} - \omega_{lo})t + \phi_{sig})}_{beat\ component} \tag{14}$$

**Doppler Velocimetry and Interferometry**

If the frequency shift in the signal is given due to Doppler velocimetry, then $\omega_{sig}=\omega_{reflected}=\omega_{incident}\left(1+\frac{2\Delta v}{c}\right)$ . In some cases it is desirable that the incident frequency be offset from the LO frequency. In such a case the following is defined: $\Delta\omega_{offset}=\omega_{incident}-\omega_{lo}$ . Substitution these relations yields the following.

$$
\begin{aligned}
I &\propto \underbrace{\frac{E_{sig}^2+E_{lo}^2}{2}}_{constant\ component} + \underbrace{E_{sig}E_{lo}\cos\left(\left(\omega_{sig}-\omega_{lo}\right)t+\phi_{sig}\right)}_{beat\ component} \\
I &\propto \frac{E_{sig}^2+E_{lo}^2}{2}+E_{sig}E_{lo}\cos\left(\left(\omega_{incident}\left(1+\frac{2\Delta v}{c}\right)-\omega_{lo}\right)t+\phi_{sig}\right) \\
I &\propto \frac{E_{sig}^2+E_{lo}^2}{2}+E_{sig}E_{lo}\cos\left(\left(\left(\omega_{lo}+\Delta\omega_{offset}\right)\left(1+\frac{2\Delta v}{c}\right)-\omega_{lo}\right)t+\phi_{sig}\right) \\
I &\propto \frac{E_{sig}^2+E_{lo}^2}{2}+E_{sig}E_{lo}\cos\left(\left(\frac{\left(\omega_{lo}+\Delta\omega_{offset}\right)2\Delta v}{c}+\Delta\omega_{offset}\right)t+\phi_{sig}\right)
\end{aligned}
\tag{15}
$$

**<u>Photon Doppler Velocimetry at Sandia</u>**

At Sandia, there exists a target with the following velocity profile.

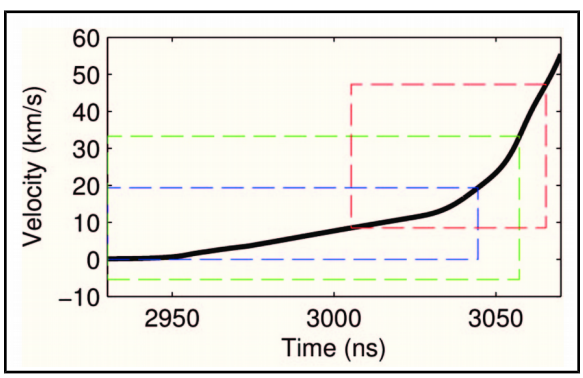


*Figure 47: PDV data of Sandia target [34].*

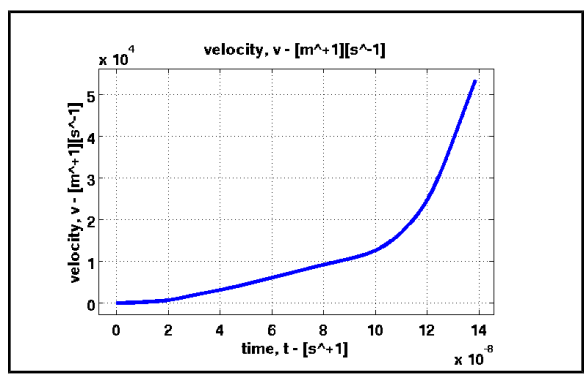


*Figure 48: Digitized PDV data of Sandia target.*

Suppose this target is irradiated with a laser having a vacuum wavelength of 1550.11198492 nm and corresponding frequency $\omega_{incident}$ . The expected Doppler frequency shift is plotted below.

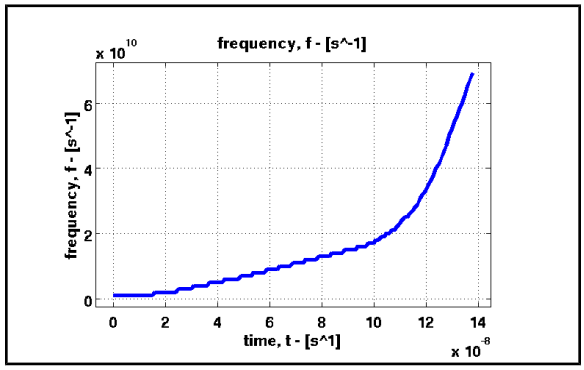


*Figure 49: Doppler frequency shift from target.*
*Note that the maximum Doppler shift is approximately 70 GHz.*

Suppose that -70 dBm of the reflected laser power is able to be collected for the entire duration of target motion. Next suppose that the reflected signal is interfered with a local oscillator laser having a vacuum wavelength of 1550.12 nm, a corresponding frequency $\omega_{lo}$, and a power of -3 dBm. Note that the laser wavelengths have been chosen such that $\Delta\omega_{offset}=1[GHz]$. After interfering the reflected signal and LO, the resulting optical signal can be described as follows.

$$P(t)=\frac{P_{sig}+P_{lo}}{2}+\sqrt{P_{sig}P_{lo}}\cos\left(\left(\frac{(\omega_{lo}+\Delta\omega_{offset})2\Delta v}{c}+\Delta\omega_{offset}\right)t+\phi_{sig}\right) \tag{16}$$

Unfortunately, the above formalism is not well suited for numerical methods. The challenge stems from discontinuities in the phase front as the frequency changes. If a continuous phase front is not maintained numerically, then phase discontinuities become manifest, introducing anomalous high-frequency artifacts. The following formalism recasts variations in the instantaneous frequency via a phase formalism to remove discontinuities.

$$P(t)=\frac{P_{sig}+P_{lo}}{2}+\sqrt{P_{sig}P_{lo}}\cos\left(\underbrace{\left(\frac{(\omega_{lo}+\Delta\omega_{offset})2\Delta v}{c}+\Delta\omega_{offset}\right)}_{\omega_{inst}(t)}t+\phi_{sig}\right) \tag{17}$$

$$\omega_{inst}(t)=\frac{(\omega_{lo}+\Delta\omega_{offset})2\Delta v}{c}+\Delta\omega_{offset} \tag{18}$$

$$\phi_{inst}(t)=\int_{-\infty}^{t}\omega_{inst}(t')dt' \tag{19}$$

$$P(t)=\frac{P_{sig}+P_{lo}}{2}+\sqrt{P_{sig}P_{lo}}\cos(\phi_{inst}(t)) \tag{20}$$

$\omega_{isnt}(t)$ is calculated using digitized velocimetry data from Figure 48. Equation (19) is calculated via numerical integration, yielding input data for equation (20). The instantaneous frequency and phase are plotted below.

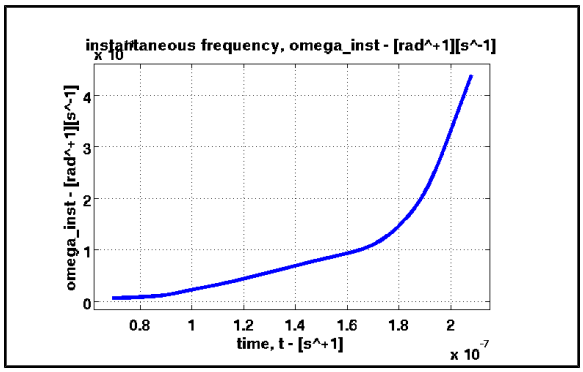


*Figure 50: Instantaneous frequency, from (18).*

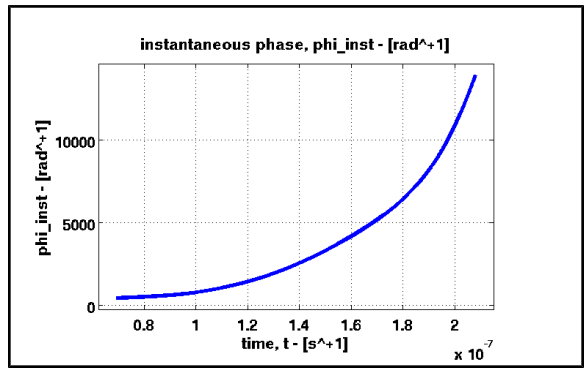


*Figure 51: Instantaneous phase, from (19).*

The optical power waveform and spectrum are plotted below.

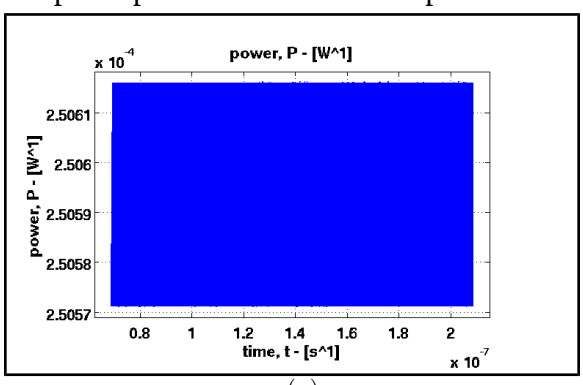


*Figure 52: $P(t)$, from (20).*

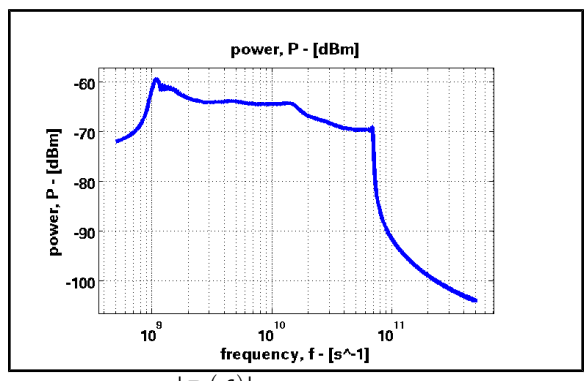


*Figure 53: $|P(f)|$, showing spectral content from 1-70 GHz.*

Finally, the short-time Fourier-transform (STFT) can reveal the time evolved frequency spectrum of $P(t)$.

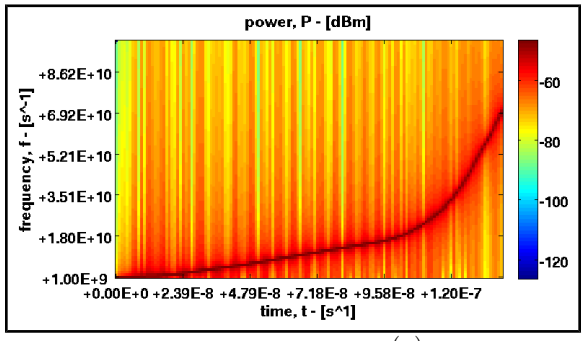


*Figure 54: STFT of* $P(t)$ .

The time-evolved Doppler shift and velocimetry data can be extracted from the STFT. First the peak of the STFT is extracted. Next the measured frequency is related to the velocity using equation (21) below.

$$\Delta v = \frac{c}{2}\frac{\omega_{inst}(t) - \Delta\omega_{offset}}{\omega_{lo} + \Delta\omega_{offset}} = \frac{c}{2}\frac{f_{inst}(t) - \Delta f_{offset}}{f_{lo} + \Delta f_{offset}} \tag{21}$$

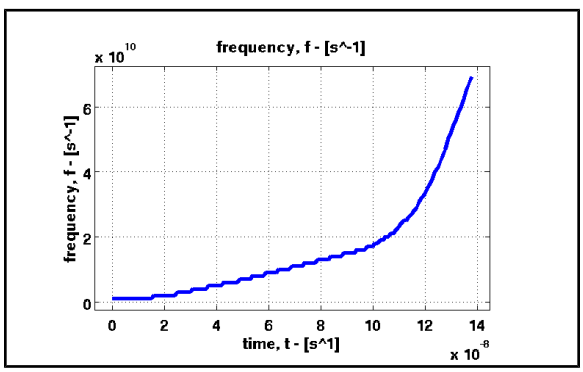


*Figure 55: Doppler shift extracted from STFT.*

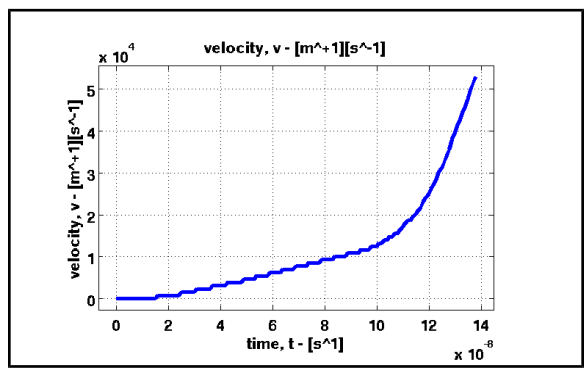


*Figure 56: Velocimetry data from STFT.*

Note that the recovered velocimetry data in Figure 56 agrees strongly with known velocimetry data in Figure 47 and Figure 48. This proves the the above described numerical PDV waveform generation method is valid. It is now possible to proceed with further analysis. Note: the discrete steps in the recovered velocimetry data are due to the discrete nature of the STFT time steps, a phenomena well known and studied in the field of PDV. These discrete steps are not central to the aims of this study, and therefore will not be discussed further. The two next

sections analyze two detection methods: (1) conventional detection, and (2) MiBo assisted detection.

## 10.2. Conventional Detection

Conventional detection consists of amplifying the optical PDV waveform via an erbium doped fiber amplifier (EDFA), followed by photodetection, DC-filtering, digitization, and digital spectral analysis via STFT. In this section, conventional detection will be simulated. The EDFA will be assumed to be noise free. The photodiode (PD) will be modeled after Finisar part number XPDV4121R. The PD has a 3 dB bandwidth of 100 GHz, and a responsivity of 0.45 A/W. The average incident optical power is set to +10 dBm. The photodiode frequency response is plotted in Figure 57, and is implemented via the linear-time-invariant (LTI) transfer function, $H(s)$, plotted in Figure 58. The photodiode also includes thermal and shot noise. The digitizer (ADC) is modeled after Tektronix part number DPO77002SX with memory option 50XL. The ADC has an analog bandwidth of 70 GHz, a sample rate of 200 GS/s, a record length of 2^30 (5 ms at 200 GS/s), 65 fs clock jitter, 8 physical bits, and 4.2 effective bits. The digitizer model implements discrete sampling and quantization to 8 physical bits. Thermal and shot noise are also implemented in the digitizer model. In this section, $P_{sig} = -70\,dBm$ and $P_{lo} = -3\,dBm$.

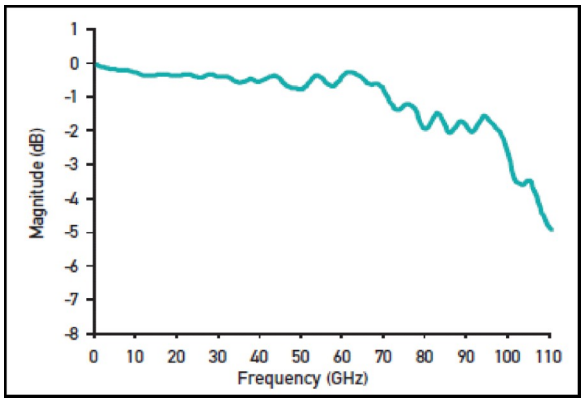


*Figure 57: Photodiode frequency response from spec sheet.*

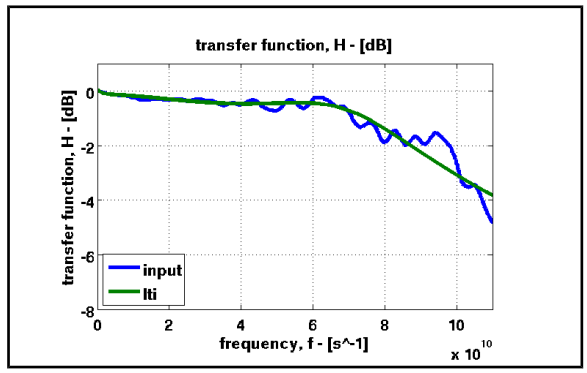


*Figure 58: Photodiode frequency response with analytical H(s) overlaid.*

The generated optical PDV waveform described in the previous section is amplified in the EDFA and made incident on the photodiode. The following electrical signal results.

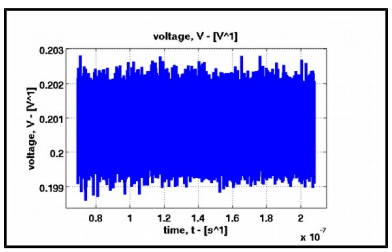


*Figure 59: PD waveform.*

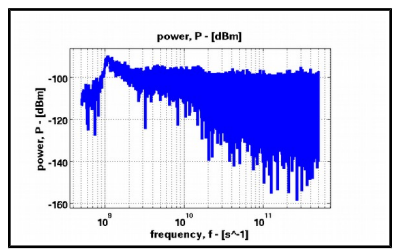


*Figure 60: PD spectrum.*

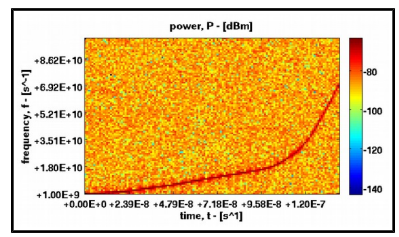


*Figure 61: STFT of PD waveform.*

The photodiode voltage waveform is passed through a lossless DC-filter and then fed to the digitizer. The following electrical signal results.

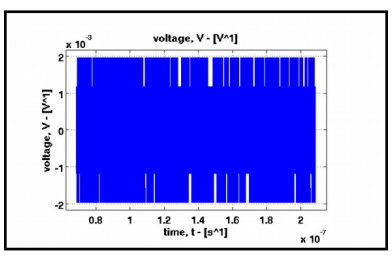


*Figure 62: Digitized waveform*

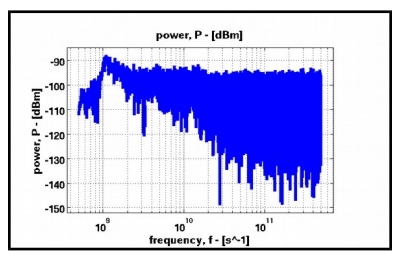


*Figure 63: Digitized Spectrum*

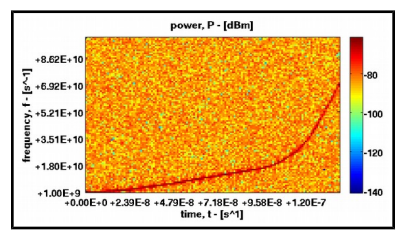


*Figure 64: STFT of Digitized waveform.*

The peak of the STFT data can be tracked to extract the Doppler frequency shift and velocimetry data.

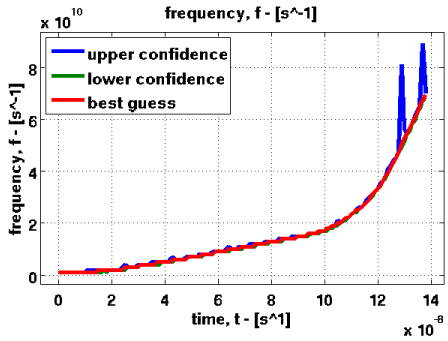


*Figure 65: Doppler shift extracted from STFT.*

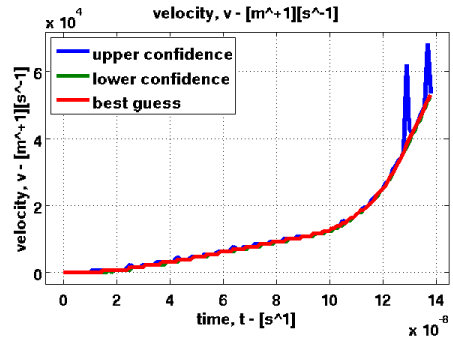


*Figure 66: Velocimetry data from STFT.*

The upper and lower confidence curves are plotted where the STFT data falls off 6 dB from the peak. In this case, the confidence is quite good, and generally tracks the peak data. Note that in this case, for the optical power levels preciously mentioned, the expected velocimetry data can be correctly recovered.

## 10.3. MiBo Assisted Detection

MiBo assisted detection proceeds similarly to the detection described in the previous section. The detected optical power levels are the same as those in the previous section. The only difference between this section and the prior is that the MiBo booster is inserted prior to photodetection. The signal and LO are combined, boosted to 400 mW in the EDFA, and are input to the 1.6 km boosting fiber, having parameters: $\alpha = 1[dB/km]$, $d = 8.7[ps/nm \cdot km]$, $s = 0.027[ps/nm^2 \cdot km]$, $\gamma = 11.6[1/W \cdot km]$. The average photodiode incident optical power is set to +10 dBm. The system schematic is below.

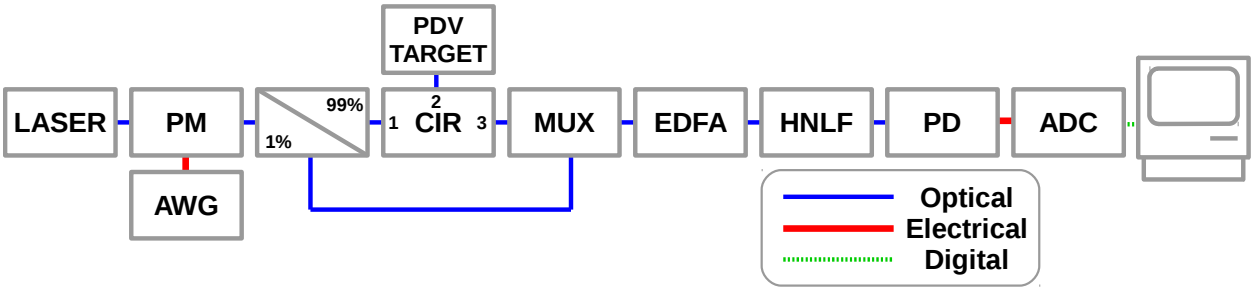


*Figure 67: System schematic*

The resultant photodiode waveforms follow.

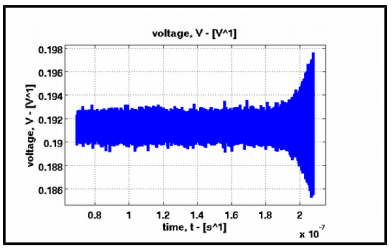


*Figure 68: PD waveform.*

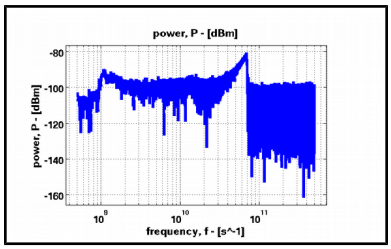


*Figure 69: PD spectrum.*

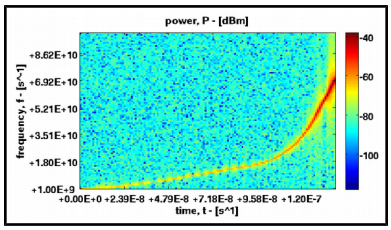


*Figure 70: STFT of PD waveform.*

The photodiode voltage waveform is passed through a lossless DC-filter and then fed to the digitizer. The following electrical signal results.

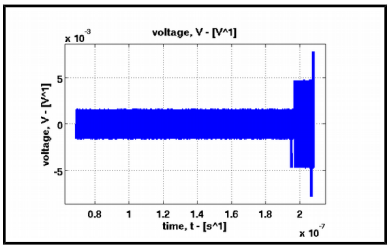


*Figure 71: Digitized waveform*

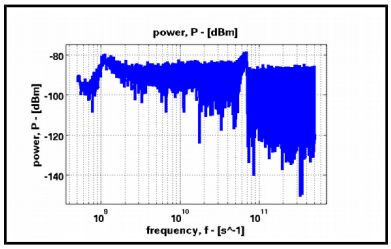


*Figure 72: Digitized Spectrum*

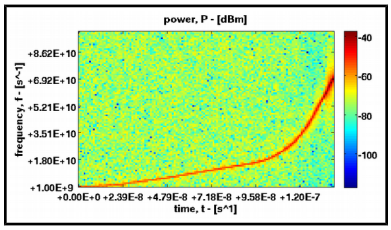


*Figure 73: STFT of Digitized waveform.*

The peak of the STFT data can be tracked to extract the Doppler frequency shift and velocimetry data.

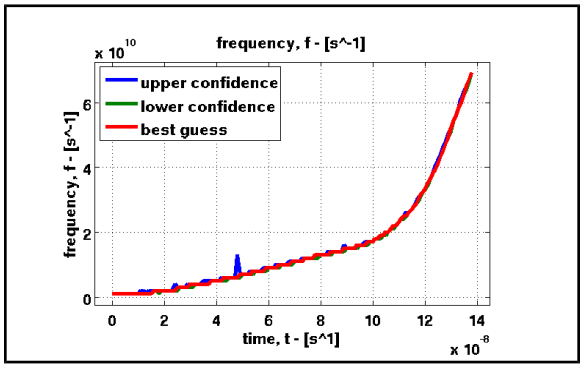


*Figure 74: Doppler shift extracted from STFT.*

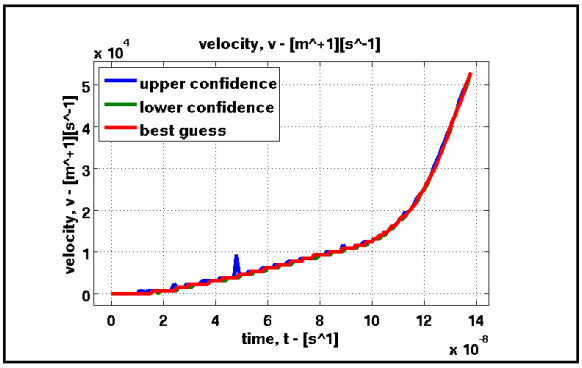


*Figure 75: Velocimetry data from STFT.*

## 10.4. Comparison

In this section conventional and MiBo assisted detection will be compared. The optical signal power will be incrementally increased and the STFT resulting from the ADC will be plotted.

| $P_{sig}[dBm]$ | Conventional | MiBo |
|---|---|---|
| -100 | 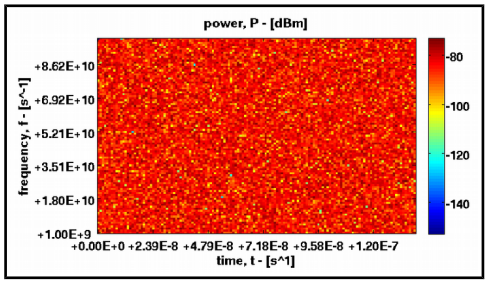 | 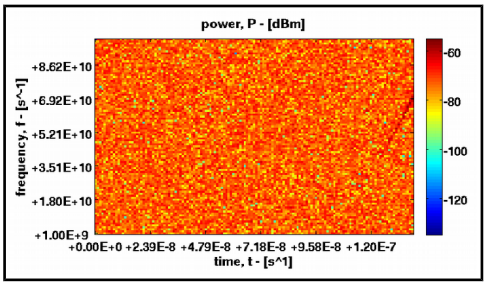 |
| -90 | 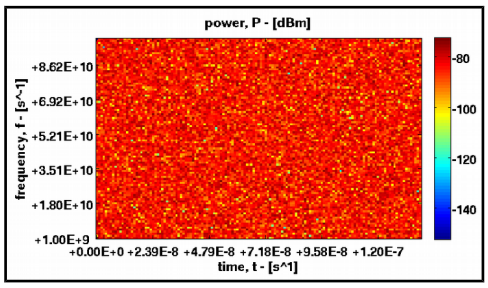 | 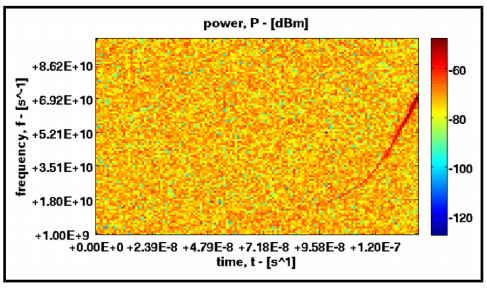 |
| -80 | 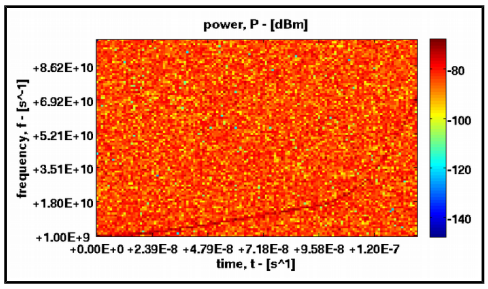 | 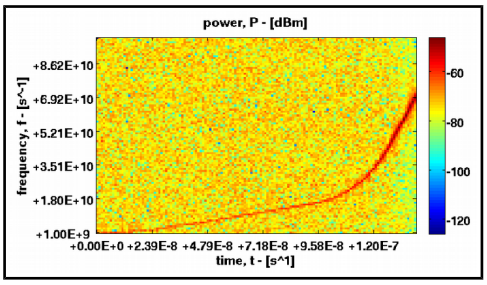 |
| -70 | 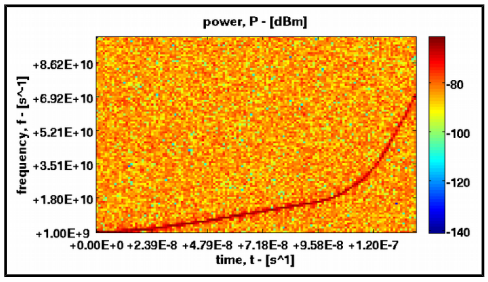 | 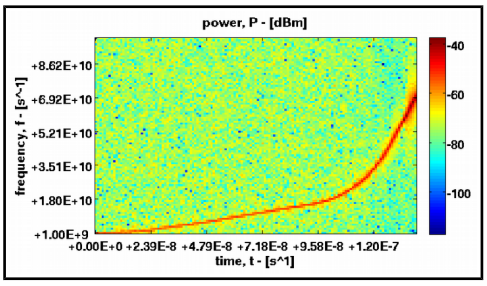 |

*Table 1: ADC STFT as a function of optical signal power for the conventional and MiBo case.*

Note that MiBo assisted detection evidences full velocimetry data with approximately 10 dB less signal power when compared to conventional detection( $MiBo(P_{sig}=-80\,dBm)$ vs $conv(P_{sig}=-70\,dBm)$ ). Also, note that MiBo evidences velocimetry data having $f>20[GHz]$ with approximately 10 dB less signal power when compared to conventional detection ( $MiBo(P_{sig}=-90\,dBm)$ vs $conv(P_{sig}=-80\,dBm)$ ). Finally, note that MiBo evidences high-speed velocimetry data having $f>40[GHz]$ with approximately 20 dB less signal power when compared to conventional detection ( $MiBo(P_{sig}=-100\,dBm)$ vs $conv(P_{sig}=-80\,dBm)$ ).

## 10.5. Discussion

Sandia's Photon Doppler Velocimetry (PDV) was described and numerically demonstrated via PDV waveform generation. Detection of this waveform via conventional detection and Modulation Index Boosted (MiBo) detection was described and numerically demonstrated. Through comparison, it was found that MiBo is 10 dB more sensitive in detecting full velocimetry information when compared to conventional detection techniques. Additionally, MiBo is able to detect challenging high-frequency (>40 GHz) velocimetry data approximately 20 dB more sensitivity than conventional detection.

Only the salient physical phenomena were modeled in this study. Therefore, only the relative performance improvement between conventional and MiBo assisted detection should be relied upon. The absolute sensitivity of PDV detection schemes requires incorporation of comprehensive technical phenomena, which may be pursued in follow-on work.

MiBo can be specifically optimized for the particular PDV frequency range of interest. At this time no such optimization has been carried out, so further performance improvements may be possible. This proof-of-principle study concretely demonstrates that MiBo can help improve PDV sensitivity, especially at high-frequencies.

## 11. Conclusion

Modulation index boosting is a new concept that exploits modulation instability to compensate for the intrinsically weak electro-optic effect, $\chi^{(2)}$. Modulation index boosting results in a highly desired reduction of the effective $V_{\pi}$ of electro-optic modulators. Simulations demonstrate more than 50-fold enhancement of electro-optic effect and modulation sensitivity at frequencies in the 100's of GHz range. Experiments have this far demonstrated 30-fold signal enhancement at 50 GHz, with the improvement trends extending to higher frequencies. Further investigations toward sensitivity improvement, frequency extension via time-stretching, and system engineering should further improve this technology. Stimulating modulation instability with RF modulation sidebands of an optical carrier enables high frequency low-voltage modulation, an increasingly critical capability that is needed if optical data communication is to keep pace with advances in electronics. Such a technology has the potential to make a tremendous improvement in technologies such as SIGINT, radar, analog, and digital communications.

## 12. References


[1] W. S. C. Chang, RF Photonic Technology in Optical Fiber Links. Cambridge: Cambridge University Press, 2002.

[2] A. Chen and E. Murphy, Broadband Optical Modulators: Science, Technology, and Applications. Boca Raton: CRC Press, 2011.

[3] Andrew Danowitz, Kyle Kelley, James Mao, John P. Stevenson, Mark Horowitz, "CPU DB: Recording Microprocessor History," ACM Queue - Processors, Volume 10 Issue 4, April (2012). doi:10.1145/2181796.2181798.

[4] K. Noguchi, O. Mitomi, and H. Miyazawa, "Millimeter-wave Ti: LiNbO3 optical modulators," Journal of Lightwave Technology, vol. 16, p. 615, 1998.

[5] Charles H. Cox III, Edward I. Ackerman, Gary E. Betts, and Joelle L. Prince, "Limits on the Performance of RF-Over-Fiber Links and Their Impact on Device Design," IEEE Transactions on Microwave Theory and Techniques, VOL. 54, NO. 2, February (2006).

[6] G. P. Agrawal, Nonlinear Fiber Optics, 4 ed. Boston: Academic Press, 2007

[7] T. B. Benjamin and J. E. Feir, "The disintegration of wave trains on deep water," Journal of Fluid Mechanics, vol. 27, pp. 417-430, 1967.

[8] H. Elbelrhiti, P. Claudin, and B. Andreotti, "Field evidence for surface-wave-induced instability of sand dunes," Nature, vol. 437, pp. 720-723, 2005.

[9] R. Bonifacio, C. Pellegrini, and L. M. Narducci, "Collective instabilities and high-gain regime in a free electron laser," Optics Communications, vol. 50, pp. 373-378, 1984.

[10] K. Tai, A. Hasegawa, and A. Tomita, "Observation of modulational instability in optical fibers," Physical Review Letters, vol. 56, pp. 135-138, 1986.

[11] K. E. Strecker, G. B. Partridge, A. G. Truscott, and R. G. Hulet, "Formation and propagation of matter-wave soliton trains," Nature, vol. 417, pp. 150-153, 2002.

[12] V. E. Zakharov and L. A. Ostrovsky, "Modulation instability: the beginning," Physica D. Nonlinear Phenomena, vol. 238, pp. 540-548, 2009.

[13] M. Hopkin, "Sea snapshots will map frequency of freak waves," Nature, vol. 430, pp. 492-492, 2004.

[14] C. Kharif and E. Pelinovsky, "Physical mechanisms of the rogue wave phenomenon," European Journal of Mechanics-B/Fluids, vol. 22, pp. 603-634, 2003.

[15] V. E. Zakharov, A. I. Dyachenko, and A. O. Prokofiev, "Freak waves as nonlinear stage of Stokes wave modulation instability," European Journal of Mechanics - B/Fluids, vol. 25, pp. 677-692, 2006.

[16] D. R. Solli, C. Ropers, P. Koonath, and B. Jalali, "Optical rogue waves," Nature, vol. 450, pp. 1054-7, Dec 13 2007.

[17] D. R. Solli, C. Ropers, and B. Jalali, "Active control of rogue waves for stimulated supercontinuum generation," Physical review letters, vol. 101, p. 233902, 2008.

[18] J. M. Dudley, G. Genty, and B. J. Eggleton, "Harnessing and control of optical rogue waves in supercontinuum generation," Optics Express, vol. 16, pp. 3644-3651, 2008.

[19] D. R. Solli, B. Jalali, and C. Ropers, "Seeded supercontinuum generation with optical parametric down-conversion," Physical review letters, vol. 105, p. 233902, 2010.

[20] P. T. S. DeVore, D. R. Solli, C. Ropers, P. Koonath, and B. Jalali, "Stimulated supercontinuum generation extends broadening limits in silicon," Applied Physics Letters, vol. 100, pp. 101111-101111-4, Mar 5 2012.

[21] J. M. Dudley, G. Genty, and S. Coen, "Supercontinuum generation in photonic crystal fiber," Reviews of Modern Physics, vol. 78, pp. 1135-1184, Oct-Dec 2006.

[22] D. R. Solli, G. Herink, B. Jalali, and C. Ropers, "Fluctuations and correlations in modulation instability," Nature Photonics, vol. 6, pp. 463-468, 2012.

[23] M. Droques, B. Barviau, A. Kudlinski, M. Taki, A. Boucon, T. Sylvestre, et al., "Symmetry-breaking dynamics of the modulational instability spectrum," Opt. Lett., vol. 36, pp. 1359-1361, 04/15 2011.

[24] N. N. Akhmediev and V. I. Korneev, "Modulation Instability and Periodic-Solutions of the Nonlinear Schrodinger-Equation," Theoretical and Mathematical Physics, vol. 69, pp. 1089-1093, Nov 1986.

[25] J. M. Dudley, G. Genty, F. Dias, B. Kibler, and N. Akhmediev, "Modulation instability, Akhmediev Breathers and continuous wave supercontinuum generation," Opt. Express, vol. 17, pp. 21497-21508, 11/23 2009.

[26] M. Taki, A. Mussot, A. Kudlinski, E. Louvergneaux, M. Kolobov, and M. Douay, "Third-order dispersion for generating optical rogue solitons," Physics Letters A, vol. 374, pp. 691-695, Jan 11 2010.

[27] G. K. Gopalakrishnan, W. K. Burns, R. W. McElhanon, C. H. Bulmer, and A. S. Greenblatt, "Performance and modeling of broadband LiNbO_3 traveling wave optical intensity modulators," Journal of Lightwave Technology, vol. 12, pp. 1807-1819, 1994.

[28] J.-M. Liu, Photonic Devices: Cambridge University Press, 2005.

[29] G. P. Agrawal, Fiber-Optic Communication Systems. New York: Wiley, 2012.

[30] C. E. Shannon, "A mathematical theory of communication," The Bell System Technical Journal, vol. 27, pp. 623-656, 1948.

[31] P. Kylemark, P. O. Hedekvist, H. Sunnerud, M. Karlsson, and P. A. Andrekson, "Noise Characteristics of Fiber Optical Parametric Amplifiers," J. Lightwave Technol., vol. 22, p. 409, 02/01 2004.

[32] J. B. Coles, et. al., "Bandwidth-efficient phase modulation techniques for Stimulated Brillouin Scattering suppression in fiber optic parametric amplifiers," Optics Express, 18(17), 18138 (2010).

[33] A. M. Fard, B. Buckley, S. Zlatanovic, C.-S. Bre, S. Radic, and B. Jalali, "All-optical time-stretch digitizer," Applied Physics Letters, Vol 101, 051113, (2012).

[34] D.H. Dolan, et. al., “Tracking an imploding cylinder with photonic Doppler velocimetry,” Review of Scientific Instruments, vol. 84, no. 055102 (2013).